

1
2
3
4 **Molecular Insights into New Particle Formation**
5 **in Barcelona, Spain**
6

7 **James Brean¹, David C.S. Beddows¹, Zongbo Shi¹,**
8 **Brice Temime-Roussel², Nicolas Marchand², Xavier Querol³,**
9 **Andrés Alastuey³, María Cruz Minguillón³, and**
10 **Roy M. Harrison^{1a*}**
11

12 **¹Division of Environmental Health and Risk Management**
13 **School of Geography, Earth and Environmental Sciences**
14 **University of Birmingham, Edgbaston, Birmingham B15 2TT**
15 **United Kingdom**
16

17 **²Aix Marseille Univ, CNRS, LCE**
18 **Marseille, 13003, France**
19

20 **³Institute of Environmental Assessment and**
21 **Water Research (IDAEA-CSIC), Barcelona, 08034 Spain**
22

23 **^aAlso at: Department of Environmental Sciences / Center of**
24 **Excellence in Environmental Studies, King Abdulaziz University, PO**
25 **Box 80203, Jeddah, 21589, Saudi Arabia**
26

* To whom correspondence should be addressed (Email: r.m.harrison@bham.ac.uk)

27 **ABSTRACT**

28 Atmospheric aerosols contribute some of the greatest uncertainties to estimates of global radiative
29 forcing, and have significant effects on human health. New particle formation (NPF) is the process
30 by which new aerosols of sub-2 nm diameter form from gas-phase precursors and contributes
31 significantly to particle numbers in the atmosphere, accounting for approximately 50% of cloud
32 condensation nuclei globally. Here, we study summertime NPF in urban Barcelona in NE Spain
33 utilising particle counting instruments down to 1.9 nm and a Nitrate CI-API-ToF. The rate of
34 formation of new particles is seen to increase linearly with sulphuric acid concentration, although
35 particle formation rates fall short of chamber studies of H₂SO₄-DMA-H₂O, while exceeding those
36 of H₂SO₄-BioOxOrg-H₂O nucleation, although a role of highly oxygenated molecules (HOMs)
37 cannot be ruled out. The sulphuric acid dimer:monomer ratio is significantly lower than that seen in
38 experiments involving sulphuric acid and DMA in chambers, indicating that stabilization of
39 sulphuric acid clusters by bases is weaker in this dataset than in chambers, either due to rapid
40 evaporation due to high summertime temperatures, or limited pools of stabilising amines. Such a
41 mechanism cannot be verified in this data, as no higher-order H₂SO₄-amine clusters, nor H₂SO₄-
42 HOM clusters were measured. The high concentrations of HOMs arise from isoprene, alkylbenzene,
43 monoterpene and PAH oxidation, with alkylbenzenes providing greater concentrations of HOMs
44 due to significant local sources. The concentration of these HOMs shows a dependence on
45 temperature. The organic compounds measured primarily fall into the SVOC volatility class arising
46 from alkylbenzene and isoprene oxidation. LVOC largely arise from oxidation of alkylbenzenes,
47 PAHs and monoterpenes, whereas ELVOC arise from primarily PAH and monoterpene oxidation.
48 New particle formation without growth past 10 nm is also observed, and on these days oxygenated
49 organic concentrations are lower than on days with growth by a factor of 1.6, and thus high
50 concentrations of low volatility oxygenated organics which primarily derive from traffic-emitted
51 VOCs appear to be a necessary condition for the growth of newly formed particles in Barcelona.
52 These results are consistent with prior observations of new particle formation from sulphuric acid-

53 amine reactions in both chambers and the real atmosphere, and are likely representative of the urban
54 background of many European Mediterranean cities. A role for HOMs in the nucleation process
55 cannot be confirmed or ruled out, and there is strong circumstantial evidence for the participation of
56 HOMs across multiple volatility classes in particle growth.

57

58

59 1. INTRODUCTION

60 Atmospheric aerosols, defined as liquid or solid droplets suspended in a gas, affect the climate both
61 directly by scattering and absorbing radiation, and indirectly by acting as cloud condensation nuclei
62 (CCN) (Penner et al., 2011), providing great uncertainties in estimates of global radiative forcing
63 (IPCC, 2014). Further, fine ambient aerosols (defined as those with diameter below 2.5 μm) are the
64 fifth greatest global mortality risk factor, resulting in 103.1 million disability-adjusted life year loss
65 in 2015 (Cohen et al., 2017). The number concentration of the ultrafine fraction of these (aerosols
66 with diameter below 0.1 μm , referred to as ultrafine particles or UFP) pose potentially significant
67 health risks also, due to their high concentration and surface area. The more diffuse, gas-like
68 behaviour of UFP allows them to penetrate into the deep lung and enter the bloodstream (Miller et
69 al., 2017). Ultrafine particles occur in the urban environment either as primary emissions (e.g., from
70 car exhaust (Harrison et al., 2018)) or secondarily as the product of new particle formation (NPF)
71 (Brines et al., 2015; Guo et al., 2014; Kulmala et al., 2017; Lee et al., 2019)

72

73 NPF is the formation of aerosol particles from gas-phase precursors. NPF can be considered a two-
74 step process involving initial formation of a cluster of gas molecules at the critical diameter at
75 around 1.5 nm - the diameter at which a free-energy barrier must be overcome to allow the
76 spontaneous phase transition from gas to liquid or solid (Zhang et al., 2012), and the subsequent
77 growth of this droplet to a larger aerosol particle. The first step of this process is dependent upon
78 the stability and abundance of the clustering molecules. Sulphuric acid, water, and dimethylamine
79 (DMA), for example, efficiently form particles as the strong hydrogen bonding between the acid
80 base pair produces near negligible evaporation, much lower than the evaporation rate seen for the
81 more weakly bound sulphuric acid-ammonia-water system. Nucleation of sulphuric acid, DMA and
82 water proceeds at, or near to the kinetic limit in a chamber at 278 K when DMA mixing ratios are
83 sufficient (Almeida et al., 2013; Kürten et al., 2014). Once past this 1.5 nm diameter, condensation
84 and coagulation will drive particle growth. Both the abundance of condensable gases and their

85 vapour pressures limit condensational growth. Vapour pressures are especially important for the
86 initial growth stages, as the Kelvin effect barrier impairs condensation of more volatile species, with
87 this condition of low vapour pressures becoming less significant as the diameter of the particle
88 increases (Tröstl et al., 2016). Once sufficiently large (>50 nm), the loss processes of coagulation
89 and evaporation of these particles become inefficient, resulting in a significant atmospheric lifetime.
90 It is from these these diameters onwards the climate forcing effects of these particles become most
91 pronounced.

92

93 NPF processes happen globally, across a diverse range of environments from pristine polar regions,
94 to polluted urban megacities (Kerminen et al., 2018), and represent a significant source of CCN,
95 with 10-60% of NPF events shown to produce CCN and enhancement factors to CCN count ranging
96 from 0.5 – 11 (Lee et al., 2019 and references within). Strong NPF events are observed across a
97 range of urban environments, despite high condensation sinks $>10^{-2} \text{ s}^{-1}$ (Bousiotis et al., 2019; Yu et
98 al., 2016), and can act as a precursor to strong haze events (Guo et al., 2014). The occurrence of
99 urban NPF has only been partially explained by growing understanding from recent in-depth studies
100 (Yao et al., 2018). Recent advances in instrumentation allow for the measurement of particles down
101 to the critical diameter with instruments such as the particle size magnifier (PSM), and (Neutral) Air
102 Ion Spectrometer (NAIS/AIS) (Lee et al., 2019), and mass spectral techniques for measuring the
103 abundance and composition of neutral (Jokinen et al., 2012) and charged (Junninen et al., 2010)
104 clusters. Elucidated mechanisms with these techniques involve sulphuric acid and ammonia in
105 remote environments (Jokinen et al., 2018; Yan, 2018), monoterpene derived highly oxygenated
106 molecules (HOM) in remote environments (Rose et al., 2018), iodic acid in coastal environments
107 (Sipilä et al., 2016), and sulphuric acid and DMA in polluted urban environments (Yao et al., 2018).

108

109 Urban Barcelona sees frequent, strong summer-time NPF events occurring on 28% of days. These
110 events are associated with high insolation and elevated ozone ($\sim 60 \mu\text{g m}^{-3}$) when considering the

111 whole year (Brines et al., 2014, 2015). Ground-level observations report NPF events starting
112 typically at midday, and either occurring in urban Barcelona and the surrounding regional
113 background simultaneously, or isolated to either urban Barcelona or just the regional background
114 (Dall'Osto et al., 2013). Vertical profiles over urban Barcelona reveal that NPF occurs at higher
115 altitudes, and starts earlier in the day, as at a given altitude these events are not suppressed by early
116 traffic peaks contributing to particle load (Minguillón et al., 2015). Here, we examine gas phase
117 mass spectral evidence and particle formation rates at the critical diameter from sulphuric acid in
118 Barcelona, with possible contribution from strong bases and highly oxygenated organic molecules
119 (HOMs), as well as factors influencing subsequent particle growth.

120

121 **2. METHODS**

122 **2.1 Sampling Site**

123 The Palau Reial site in Barcelona (41°23'15" N, 2°6'53.64" E) is representative of the urban
124 background of Barcelona, located at the Institute of Environmental Assessment and Water Research
125 (IDAEA-CSIC) in the north-west of the city. Sampling was performed from a container 20 m from
126 a low traffic road, and 200 m from the nearest main road (Avinguda Diagonal). Data were taken
127 from 2018/06/28 through 2018/07/18.

128

129 **2.2 Chemical Ionisation Atmospheric Pressure Interface Time of Flight Mass**

130 **Spectrometry**

131 The Aerodyne Nitrate Chemical Ionisation Atmospheric Pressure interface Time of Flight Mass
132 Spectrometer (CI-APi-ToF) was used to make measurements of neutral oxygenated organic
133 compounds, organic and inorganic acids, bases, and their molecular clusters at high time resolution
134 with high resolving power. The ionization system charges molecules by adduct formation, such as
135 in the case of organic compounds with two or more hydrogen bond donor groups (Hytinen et al.,
136 2015), or proton transfer in the case of strong acids like sulphuric acid (Jokinen et al., 2012).

137 Hydroxyl or hydroperoxyl functionalities are both common hydrogen bond donating groups, with
138 hydroperoxyl being the more efficient hydrogen bond donor (Møller et al., 2017). This instrument
139 has been explained in great detail elsewhere (Jokinen et al., 2012; Junninen et al., 2010), but briefly,
140 the front end consists of a chemical ionisation system where a 10 L min^{-1} sample flow is drawn in
141 through the 1 m length 1" OD stainless steel tubing opening. A secondary flow was run parallel and
142 concentric to this sample flow, rendering the reaction chamber effectively wall-less. A $3 \text{ cm}^3 \text{ min}^{-1}$
143 flow of a carrier gas (N_2) is passed over a reservoir of liquid HNO_3 , entraining vapour which is
144 subsequently ionised to NO_3^- via an X-ray source. Ions are then guided into the sample flow. The
145 nitrate ions will then charge molecules either by clustering or proton transfer. The mixed flows
146 travelling at 10 L min^{-1} enter the critical orifice at the front end of the instrument at 0.8 L min^{-1} and
147 are guided through a series of differentially pumped chambers before reaching the ToF analyser. All
148 data analysis was carried out in the Tofware package in Igor Pro 7 (Tofwerk AG, Switzerland).
149 Signals except for those of amines and ammonia are divided by the sum of reagent ion signals and
150 multiplied by a calibration coefficient to produce a concentration. A calibration coefficient of 3×10^9
151 cm^{-3} was established based upon comparison with a sulphuric acid proxy (Mikkonen et al., 2011)
152 and is in line with a prior calibration with our instrument (Brean et al., 2020). Uniform sensitivity
153 between H_2SO_4 and all other species measured by CI-APi-ToF bar amines and ammonia was
154 assumed in this work. This introduces some uncertainties, as it relies upon both collision rates and
155 charging efficiencies to be the same within the ionisation source for all species. Amine and
156 ammonia signals are normalised to the nitrate trimer signal (Simon et al., 2016). Prior reports of
157 ammonia and amines as measured by CI-APi-ToF employed corona discharge systems, which
158 utilise higher concentrations of nitric acid, thus we report normalised signals. We present
159 correlations of each of these bases clustered with the nitrate dimer plotted against measurements
160 with the nitrate trimer, as well as their intercorrelations and example peak fits across Figure S1. C_2
161 amines, C_4 amines and ammonia were the only molecules of this kind found in our mass spectra.
162 Systematic uncertainties of +100% / -50 % arising from this method are assumed.

163 Due to the high resolving power of the CI-APi-ToF system (mass resolving power of 3000, and
164 mass accuracy of 20 ppm at 201 m/Q), multiple peaks can be fit at the same unit mass and their
165 molecular formulae assigned. Beyond 500 m/Q, peak fitting and assignment of compositions
166 becomes problematic as signal decreases, mass accuracy decreases, and the total number of possible
167 chemical compositions increases, so peaks above the C₂₀ region have not been assigned (Cubison
168 and Jimenez, 2015), however, signals past this region tended to be extremely low. All ions
169 identified are listed in Table S1. As proton transfer mostly happens with acids, and nearly all HOM
170 molecules will be charged by adduct formation it is possible to infer the uncharged formula;
171 therefore, all HOMs from here onwards will be listed as their uncharged form. The CI-APi-ToF
172 inlet was placed approximately 1.5 m a.g.l. CI-APi-ToF data is only available between the dates
173 2018/07/06 and 2018/07/17.

174

175 **2.2 Particle Size and Number Measurements**

176 Two Scanning Mobility Particle Sizer (SMPS) instruments measured particle size distributions at 5
177 minute time resolution, one Long Column SMPS (TSI 3080 EC, 3082 Long DMA, 3772 CPC, TSI,
178 USA) and one NanoSMPS (3082 EC, 3082 Nano DMA, 3776 CPC, TSI, USA) measuring the
179 ranges 10.9 – 478.3 nm and 4.5 – 65.3 nm respectively. A Particle Size Magnifier (A10, Airmodus,
180 FN) linked to a CPC (3775, TSI, USA) measured the sub-3 nm size fraction. The PSM was run in
181 stepping mode, operating at four different saturator flows to vary the lower size cut of particles that
182 it will grow (defined as the point of 50% efficiency, D₅₀). The instrument provided D₅₀ from 1.4 to
183 2.4 nm. The instrument switched between saturator flows each 2.5 minutes, giving a sub-2.4 nm
184 size distribution every 10 minutes. Aerosol sampling inlets were placed approximately 2 m a.g.l.

185

186 **2.3 Other Measurements**

187 Mixing ratios of non-methane VOC with proton affinity greater than H₃O⁺ were made using the
188 proton transfer reaction time of flight mass spectrometer (PTR-ToF-MS 8000, Ionicon Analytik

189 GmbH, Austria). A detailed description of the instrument is provided by Graus et al., (2010) The
 190 sampling set up, operating conditions, and quantification procedures are similar to those described
 191 in Minguillón et al. (2016). Continual monitoring of composition and mass of submicron aerosol
 192 >75 nm was carried out with an Aerosol Chemical Speciation Monitor (ACSM, Aerodyne, USA)
 193 (Ng et al., 2011). Ozone, NO, and NO₂ were measured by conventional ultraviolet and
 194 chemiluminescence air quality instrumentation. Meteorological data were supplied by the Faculty of
 195 Physics of University of Barcelona, from a nearby (200 m from the measurement site)
 196 meteorological station located at the roof of an 8 floor building.

197

198 **2.4 Condensation Sink and Particle Growth Rate**

199 The condensation sink (CS) represents the rate at which a vapour phase molecule will collide with
 200 pre-existing particle surface, and was calculated from the size distribution data as follows (Kulmala
 201 et al., 2012):

202

$$203 \quad CS = 2\pi D \sum_{d_p} \beta_{m,d_p} d_p N_{d_p}, \quad (1)$$

204

205 where D is the diffusion coefficient of the diffusing vapour (assumed sulphuric acid), β_m is a
 206 transition regime correction (Kulmala et al., 2001), d_p is particle diameter, and N_{d_p} is the number of
 207 particles at diameter d_p . The formation rate of new particles at size d_p is calculated as follows:

208

$$209 \quad J_{d_p} = \frac{dN_{d_p}}{dt} + CoagS_{d_p} \cdot N_{d_p} + \frac{GR}{\Delta d_p} \cdot N_{d_p} \quad (2)$$

210

211 where the first term on the right-hand side comprises the rate at which particles enter the size d_p ,
 212 and the latter two terms represent losses from this size by coagulation and growth respectively. J_5
 213 was calculated using the data in the range of 5 – 10 nm, and $J_{1.9}$ was calculated using the
 214 measurements in the range of 1.9 – 4.5 nm. We also calculated $J_{1.9}$ from our NanoSMPS data,

215 employing the equations of Lehtinen et al. (2007). $J_{1.9}$ from both methods showed reasonable
216 agreement ($R^2 = 0.34$). Agreement between J_5 and $J_{1.9}$ for each method was similar ($R^2 = 0.37$ and
217 $R^2 = 0.38$ for $J_{1.9}$ calculated from PSM data and from Lehtinen et al. (2019) respectively). $J_{1.9}$ is
218 greater than J_5 as predicted from equation (2) by around a factor of 20. See Kulmala et al. (2001) for
219 more information on calculation of coagulation sinks and formation rates. Growth rates in the range
220 of 4.5 – 20 nm were calculated according to the lognormal distribution function method (Kulmala et
221 al., 2012), whereas those in the range of 1.9 – 4.5 nm were calculated from PSM data using a time-
222 delay method between PSM and NanoSMPS data. Systematic uncertainties on our calculated $J_{1.9}$
223 values include 25% method uncertainty (Yli-Juuti et al., 2017), with a further 25% arising from
224 uncertainties in PSM cutoff (± 0.5 nm), as well as a 10% uncertainty in counting errors. A 50%
225 error arising from calculated coagulation sink is also applied (Kürten et al., 2016). The above
226 calculations rely on the assumption of homogeneous air masses, and while air mass advection, as
227 well as primary particle emissions can cause errors in estimations of temporal changes in particle
228 count and diameter, the appearance and persistence of a new mode of particles across a period of
229 several hours is typically indicative of a regional process.

230

231 Growth rates from irreversible condensation of various vapours were calculated as according to
232 Nieminen et al. (2010). At our measured relative humidity, sulphuric acid favours binding to 2 H₂O
233 molecules (Kurtén et al., 2007). As amine concentrations are likely limited, we presume no mass
234 from amines in the condensing species. H₂SO₄ was assigned a density of 1.8 g cm⁻³. For simplicity,
235 the properties of MSA regarding density and hydration were presumed the same as H₂SO₄, and
236 HIO₃ was presumed to have the same hydration as H₂SO₄, with a density of 4.98 g cm⁻³. The
237 density of condensing organic vapours was assumed 1.5 g cm⁻³, and concentration-weighted mean
238 mass (~ 276 g mol⁻¹ for LVOC) and atomic weighted diffusion volumes of organic compounds were
239 used to calculate GRs.

240

241 **2.4 DBE and 2D-VBS**

242 The double bond equivalent (DBE) describes the degree of unsaturation of an organic molecule and
243 is defined simply as:

244

$$245 \quad DBE = N_C - \frac{N_H}{2} - \frac{N_N}{2} + 1 \quad (3)$$

246

247 The saturation vapour pressure at 300 K is defined by the 2D-volatility basis set (2D-VBS) as
248 follows, if all nitrogen functionality is assumed to take the form -ONO₂ (Bianchi 2019; Donahue
249 2011; Schervish and Donahue, 2020):

250

$$251 \quad \text{Log}_{10}(C^*)(300 \text{ K}) = (N_{C0} - N_C)b_C - N_O b_O - 2 \frac{N_O N_C}{N_C + N_O} b_{CO} - N_n b_N \quad (4)$$

252

253 where N_C , N_H , and N_N , are the number of carbon, hydrogen, and nitrogen atoms respectively. N_O is
254 the number of oxygen atoms minus $3N_N$ to account for -ONO₂ groups, N_{C0} is 25 (the carbon
255 number of an alkane with a saturation mass concentration of $1 \mu\text{g m}^{-3}$), b_C , b_O , b_{CO} , and b_N are
256 0.475, 0.2, 0.9 and 2.5 respectively, and represent interaction and nonideality terms. The final term
257 of equation (4) accounts for -ONO₂ groups, each reducing the saturation vapour pressure by 2.5
258 orders of magnitude. C^* values are calculated at 300 K and not corrected for temperature, as 300 K
259 is within 1 K of the campaign average temperature.

260

261 **3. RESULTS AND DISCUSSION**

262 **3.1 General Conditions of NPF Events**

263 Summer NPF events in the regional background around Barcelona are associated with high
264 insolation, relatively low ozone concentration (high compared with the rest of the year), and lower
265 particulate matter load (Brines et al., 2014; Carnerero et al., 2019). Figure 1 shows an example of a
266 day with no NPF in panel (a), referred to as “non-event” here, where two traffic-associated peaks in

267 particle number are seen during rush hours. Midday traffic peaks are also seen on certain days, but
268 these are easily distinguished from nucleation processes due to the lack of a significant <10 nm
269 mode. Figure 1(b) shows a nucleation day with growth to larger sizes >10 nm, termed “full-event”,
270 showing the growth through the course of the day. These fulfil all the criteria of Dal Maso et al.
271 (2005). 4 events of this type were observed with CI-API-ToF data coverage. Figure 1(c) shows a
272 day with nucleation occurring, but no growth past 10 nm. These days are referred to as “burst-
273 event” days. Here, NPF is seen to occur, but particles fail to grow past the nucleation mode. 2 such
274 events were seen in this data with CI-API-ToF data coverage, and both are accompanied by a
275 distinct mode appearing beforehand in the range of ~20 – 40 nm. Condensation sinks were not
276 significantly higher than on full event days, so this failure of particles to grow further cannot be
277 attributed to condensational (or coagulation) losses. $GR_{4.5-20}$ ranged between 2.47 and 7.31 nm h^{-1}
278 ($4.69 \pm 2.03 \text{ nm h}^{-1}$), $GR_{1.9-4.5}$ ranged between 3.12 and 5.20 nm h^{-1} ($4.36 \pm 1.02 \text{ nm h}^{-1}$). The
279 survival parameter (P) as suggested by Kulmala et al. (2017) is defined as $CS \cdot 10^{-4} / GR$, and for this
280 data is equal to 41, higher than other European cities.

281

282 Figure 2 contains box plots showing condensation sink, temperature and global radiation for all 3
283 NPF types across the entire day (diurnal profiles plotted in Figure S2). Condensation sinks during
284 NPF periods of both types (Figures 1(b) & 1(c)) were not significantly lower than in non-event
285 periods. Condensation sinks were suppressed prior to the beginning of an event for full-events,
286 increasing relative to non-events through the afternoon period. Of the two burst-events, one was
287 similarly characterised by a suppression to condensation sink, whereas the other showed a sharp rise
288 in the midday. Global radiation and temperature were higher for full-events, most significantly for
289 temperature. Figure 3 is as Figure 2 but for sulphuric acid, ammonia and amines, and HOMs as
290 measured by CI-API-ToF (HOM criteria are discussed in section 3.3.1). Sulphuric acid is elevated
291 during both full-event and burst-event periods. In urban Barcelona, sulphuric acid will primarily
292 arise from oxidation of SO_2 by the OH^\cdot radical, with anthropogenic emissions such as shipping

293 emissions from the port areas being significant sources of SO₂ (Henschel et al., 2013). Direct traffic
294 emissions have been shown to be a significant primary sulphuric acid source (Olin et al., 2020), but
295 our sulphuric acid data show no traffic peaks. Ammonia and amines show enhancement for full-
296 event periods, but not burst-event periods. Nucleation rates (at typical tropospheric sulphuric acid
297 concentrations) are sensitive to amine concentrations in the range of a few pptv, with enhancements
298 to amine mixing ratios past this point increasing the nucleation rate marginally (Almeida et al.,
299 2013), while typical concentrations of DMA and other alkylamines vary from zero to a few pptv in
300 the boundary layer (Ge et al., 2011a).

301

302 Barcelona has been shown to contain ppbv levels of ammonia (Pandolfi et al., 2012), arising from
303 both agriculture to the north (Van Damme et al., 2018), and anthropogenic activities such as waste
304 management and traffic, with waste management being the primary ammonia source. Highest
305 ammonia mixing ratios are found in the densely populated old city centre (Reche et al., 2015).
306 Agriculture, waste management, and traffic are also all significant sources of low molecular weight
307 alkylamines, such as DMA (Ábalos et al., 1999; Cadle and Mulawa, 1980; Hutchinson et al., 1982;
308 Ge et al., 2011a), and are likely the source of amines found in this dataset. Activities such as
309 composting and food industry are especially strong sources of trimethylamine (TMA) (Ge et al.,
310 2011a). Although high emission fluxes of TMA are expected in this environment, they are not
311 present in our spectra. The TMA ion has been reported previously with a similar ionisation setup to
312 that utilised in this study (Kürten et al., 2016). On full-event days, the signal for C₂ and C₄ amines
313 has a midday elevation concurrent with peaks to solar radiation (Figure S2), and can help explain
314 the high formation rates we see in this dataset (see section 3.2). The relative strength of these
315 signals are shown in Figure S3, with significantly higher signals attributed to ammonia compared to
316 amines, despite a likely lower sensitivity (Simon et al., 2016).

317

318 HOM concentrations were greatly enhanced during full-event periods (factor of 1.5 higher
319 compared to non-NPF mean), but lower during burst-event periods (factor of 1.2 lower compared to
320 non-NPF mean), implying their necessity for growth. The sources and implications of these HOMs
321 are discussed in section 3.3. Further, concentrations of iodine and DMS-derived acids such as iodic
322 acid (HIO_3) and methanesulphonic acid (MSA) are low ($7.8 \cdot 10^5$ and $3.3 \cdot 10^5 \text{ cm}^{-3}$ respectively),
323 indicating a small influence of oceanic emissions on particle nucleation/growth. Extended box plots
324 as Figures 2 & 3 are presented in Figure S4, and HYSPLIT back trajectories per event in Figure S5.

325

326 **3.2 Mechanisms of New Particle Formation**

327 The correlation between $J_{1,9}$ and concentration of sulphuric acid is plotted in Figure 4. A close
328 relationship between nucleation rates and sulphuric acid concentrations ($R^2 = 0.49$) are consistent
329 with observations globally (Lee et al., 2019). This relationship is not dependent upon condensation
330 sink. These NPF rates have no dependence on other ions as measured by CI-Api-ToF, including
331 HIO_3 , MSA, ammonia, amines or HOMs (R^2 for all < 0.1). This is not to say that all of these
332 molecules are not involved in the nucleation process, rather that elevations or reductions to their
333 concentrations during nucleation periods do not have significant impact on nucleation rates. In the
334 example of alkylamines, their gas phase concentration may decrease due to clustering with elevated
335 sulphuric acid, as they cluster at around a 1:1 ratio at high amine mixing ratios (Kürten et al., 2014)
336 (and therefore they will not be detectable as free amines). Further, if amines are present at a few
337 pptv, their mixing ratios are significantly higher than our ambient measured sulphuric acid
338 concentrations, and will be sufficient to accelerate nucleation rates (Almeida et al., 2013).
339 Photochemical losses will also be greater during the periods of highest NPF rate (Ge et al., 2011b).
340 The strength of the relationship between sulphuric acid and nucleation rate has been quantitatively
341 reproduced in chamber studies involving the $\text{H}_2\text{SO}_4\text{-H}_2\text{O-DMA}$, and $\text{H}_2\text{SO}_4\text{-H}_2\text{O-BioOxOrg}$
342 system, accurately reproducing tropospheric observations of nucleation rates (Almeida et al., 2013;
343 Riccobono et al., 2014), although a later revision of the former shows nucleation rates at 278 K

344 exceeding typical tropospheric observations in the presence of high mixing ratios of DMA (Kürten
345 et al., 2018). A comparison between our data and results from the CLOUD chamber is presented in
346 Figure 5; included are the H₂SO₄-H₂O, H₂SO₄-NH₃-H₂O (Kirkby et al., 2011), H₂SO₄-H₂O-DMA
347 (Kürten et al., 2018) and H₂SO₄-BioOxOrg-H₂O systems (Riccobono et al., 2014) – BioOxOrg
348 refers to the oxidation products of pinanediol (C₁₀H₁₈O₂) and OH. Data from these chamber
349 experiments is for 278 K and 38 – 39 % relative humidity. Nucleation rates measured in Barcelona
350 ($J_{1.9} 178 \pm 190 \text{ cm}^{-3} \text{ s}^{-1}$ at $[\text{H}_2\text{SO}_4] 7.1 \cdot 10^6 \pm 2.7 \cdot 10^6 \text{ cm}^{-3}$) are around an order of magnitude lower
351 than that seen for the H₂SO₄-DMA-H₂SO₄ system, but exceed that of the H₂SO₄-BioOxOrg-H₂O
352 system by ~1 order of magnitude, and that of the H₂SO₄-NH₃-H₂O and H₂SO₄-H₂O system multiple
353 orders of magnitude. No dissimilarity is seen between the data points corresponding to full or burst
354 type nucleation, indicating similar mechanisms of formation, despite lower HOM concentrations on
355 burst-event days. Conversely, research in remote boreal environments show that the mechanism of
356 nucleation can modulate dependent upon the H₂SO₄:HOM ratio (Yan et al., 2018). Model studies of
357 sulphuric acid-amine nucleation show a decline in nucleation rate with an increasing temperature
358 (Almeida et al., 2013; Olenius et al., 2017), as the evaporation rate of sulphuric acid-amine clusters
359 will increase with temperature (Paasonen et al., 2012). Conversely, evaporation rates of such small
360 clusters, and resultant nucleation rates tend to increase modestly with increases in relative humidity,
361 most pronounced at lower amine concentrations (Almeida et al., 2013; Paasonen et al., 2012).
362 Despite this, high nucleation rates at temperatures nearing 300 K have been reported previously
363 (Kuang et al., 2008; Kürten et al., 2016), although these tend to show a temperature dependence
364 (Yu et al., 2016). No higher-order sulphuric acid clusters, sulphuric acid-base clusters, nor
365 sulphuric acid-HOM clusters were visible in the mass spectral data, likely due to these being below
366 the limit of detection of the instrument (Jokinen et al., 2012), so cluster identity cannot be directly
367 identified. Sulfuric acid trimer stabilisation is dependent upon base abundance (Ortega et al 2012),
368 and conversely, sensitivity of nitrate CI-Api-ToF to sulfuric acid-base clusters is reduced due to the
369 high base content of such clusters (Jen et al., 2016).

370 To further explore the relationship between sulphuric acid clusters and the rate of nucleation, the
371 sulphuric acid dimer:monomer ratio is plotted in Figure 6. The sulphuric acid dimer:monomer ratio
372 is elevated by the presence of gas-phase bases such as DMA, and this elevation is dependent upon
373 both the abundances and proton affinities of such bases (Olenius et al., 2017). Upon charging,
374 evaporation of water and bases from sulphuric acid clusters occurs, and thus these are detected as
375 sulphuric acid dimer (Ortega et al., 2012, 2014). The binding energy of the bisulphate-H₂SO₄ ion is
376 in excess of 40 kcal mol⁻¹ (Curtius et al., 2001), and thus minimal declustering of the dimer is
377 expected within the CI-Api-ToF instrument – however, declustering of higher order sulphuric acid
378 clusters has been shown to be sensitive to voltage tune (Passananti et al., 2019), and this likely
379 extends to the dimer also, and as such discrepancies between sets of results due to instrument setup
380 cannot be ruled out. The ratio of sulphuric acid dimer:monomer is also highly sensitive to
381 condensation sinks, with a difference in dimer concentration of approximately a factor of 4
382 expected at 10⁷ cm⁻³ between 0.001 s⁻¹ (a clean environment) and 0.03 s⁻¹ (condensation sinks
383 during these NPF events measured in this dataset) (Yao et al., 2018) and thus our low
384 dimer:monomer ratio can, in part, be explained by elevated condensation sinks. The dashed line
385 represents the ratio that would be seen due to ion induced clustering (IIC) in the nitrate chemical
386 ionisation system for a 50 ms reaction time (Zhao et al., 2010). The sulphuric acid dimer:monomer
387 ratio seen in the CLOUD H₂SO₄-DMA-H₂O system is plotted, alongside our own data from
388 Barcelona. The ratio from our own data is seen to be much lower than that for the system purely
389 involving DMA as a ternary stabilising species. Similarly, this ratio is lower than for reports of
390 H₂SO₄-DMA-H₂O nucleation in Shanghai (Yao et al., 2018), but is markedly similar to reports in
391 central rural Germany (Kürten et al., 2016). Similar to central Germany, this ratio increases at lower
392 sulphuric acid concentrations to a ratio more similar to the H₂SO₄-DMA-H₂O system. A possible
393 explanation for this is that at higher sulphuric acid concentrations, the concentrations of stronger
394 stabilising bases are insufficient to stabilise all present sulphuric acid, with the higher end of the
395 sulphuric acid concentrations seen in this data roughly equivalent to 1 pptv sulphuric acid (3×10⁷

396 $\text{cm}^{-3} = 1.2 \text{ pptv}$ sulphuric acid). We also cannot account for clustering due to naturally charged
397 sulphuric acid in the atmosphere, but ion concentrations in urban environments tend to be small due
398 to efficient sink processes (Hirsikko et al., 2011). Particle formation plausibly operates by sulphuric
399 acid-amine nucleation involving the measured C_2 and C_4 amines in our data, with nucleation rates
400 hindered relative to those measured in the CLOUD experiments by elevated temperatures, and a
401 decline to the sulphuric acid dimer:monomer ratio indicates that base concentrations may be
402 limited. We cannot rule out an involvement of HOMs in particle formation processes, and, as no
403 higher-order clusters were observed, we cannot establish sulphuric acid-amine nucleation with
404 certainty.

405

406 **3.3 HOMs and Growth**

407 **3.3.1 HOM composition and sources**

408 Barcelona, as a densely populated urban agglomerate, is distinct from the remote conditions under
409 which HOMs have primarily been studied (Bianchi et al., 2016, 2017; Schobesberger et al., 2013;
410 Yan et al., 2016), and is characterised by elevated temperatures, insolation and NO_x mixing ratios,
411 as well as a diverse host of potential precursor VOC. The first of these affects HOM yields
412 significantly, as yields are highly dependent upon temperature (Quéléver et al., 2019; Stolzenburg et
413 al., 2018). Lower temperatures result in slower H-abstractions, which will result in the likelihood of
414 an RO_2 To undergo a different reaction pathway, such as termination with HO_2 To increase (Praske
415 et al., 2018). This is particularly important in this study if there is a large energy barrier for the first
416 or second H-abstraction taking place, as this will determine the number of hydrogen bond donating
417 groups, and therefore whether the NO_3^- CI-API-ToF is sensitive to a molecule or not. Elevated
418 insolation will result in enhanced photochemistry, and thus more rapid RO_2 Formation rates,
419 whereas elevated NO_x will produce more HOM with nitrate ester functionality (Garmash et al.,
420 2020; Rissanen, 2018), which tend towards higher volatilities, and less efficient participation in
421 particle formation (Ehn et al., 2014; Lehtipalo et al., 2018), and growth (Yan et al., 2020).

422

423 Oxygenated volatile organic compounds (OVOC) are defined as species visible in the nitrate CI-API-
424 ToF that do not classify as HOM. Here, the first of the three criteria provided by Bianchi et al. (2019),
425 that HOM must be formed by peroxy radical autoxidation, cannot be applied to define HOM, as
426 knowledge as to whether a molecule is a result of autoxidation requires sound knowledge of the
427 structure of the precursors, oxidants and peroxy radical terminators present, however, the number of
428 molecules observed with $N_n = 2$ is around an order of magnitude lower than that for $N_n = 1$, where
429 the primary source of multiple nitrogen functionalities would be multiple peroxy radical termination
430 reactions from NO_x , and therefore while multiple generations of oxidation have been shown to occur
431 in aromatics (Garmash et al., 2020), it is a small contributor to the concentration of what is classed as
432 HOM here. The second criterion to define HOM are that they must be formed in the gas phase under
433 atmospherically relevant conditions, which we deem appropriately fulfilled as all CI-API-ToF
434 measurements are of gas phase compounds, and the final criterion is that HOM must contain more
435 than 6 oxygen atoms. To attempt to satisfy these criteria as best possible, the criteria of both
436 containing 6 oxygen atoms and 5 carbon atoms or greater and having an O:C ratio >0.6 is applied.

437

438 The diversified range of HOM precursors in Barcelona will be primarily anthropogenic in origin.
439 Averaged PTR-MS mixing ratios of different VOCs are presented in Figure S6. Figure 7(a) shows
440 HOM concentration plotted against temperature, showing a dependence of HOM concentrations on
441 temperature, with a lesser dependence on global radiation. The precursors for these HOMs are
442 presumed to be largely isoprene, alkylbenzenes, monoterpenes, and PAHs. The mean peak
443 intensities assigned to alkylbenzene derived HOMs are approximately a factor of two higher than
444 those assigned to isoprene and monoterpene oxidation across this entire campaign. In this data these
445 VOC mixing ratios are, with the exception of isoprene, not largely temperature dependent, with
446 many of these HOMs forming under negligible or zero insolation, and therefore very low OH
447 concentrations. These nighttime HOMs will not be derived from the oxidation of aromatics,

448 however, as rates of oxidation of alkylbenzenes by O_3 and NO_3 are negligible (Molteni et al,
449 2018). These nighttime HOMs will therefore mostly be derived from biogenic emissions which
450 undergo more rapid nocturnal oxidation, and are likely transported from inland by the land breeze
451 during night (Millán, 2014; Querol et al., 2017).

452

453 Operating under the assumption that C_5 , C_6 , C_7 , C_8 , and C_9 HOMs primarily arise from isoprene,
454 benzene toluene, C_2 -alkylbenzene C_3 -alkylbenzene oxidation respectively (Massoli et al., 2018;
455 Molteni et al., 2018; Wang et al., 2017), HOM signals plotted against parent VOC concentration
456 indicate their dependence upon that VOC. Here, a C_7 HOM is thought to follow the formula C_7H_8
457 $_{12}O_{5-10}N_{0-2}$. We have plotted HOM concentrations against VOC concentrations in Figure 7(b). C_{10}
458 HOMs are not included in these analyses as these may primarily arise from $C_{10}H_{12-14}$ alkylbenzene,
459 or monoterpene oxidation. HOM concentration appears mostly independent of VOC concentration,
460 with the exception of isoprene, for which emissions are highly temperature dependent, and thus this
461 is likely a function of the effect of temperature on HOM formation (Figure 7(a)). A lack of
462 correlation between other VOCs and their HOMs confirms that this relationship between HOMs
463 and temperature is not a function of enhanced VOC emission fluxes from, for example, evaporation,
464 except in the instance of isoprene. Fragmented monoterpene oxidation products will also contribute
465 to the total number of C_9 HOMs, and similarly, other VOCs can fragment upon oxidation. However,
466 these results indicate that HOM concentrations are elevated by temperature, and operate quite
467 independent of precursor VOC concentration.

468

469 DBE as calculated by equation 3 is equal to the number of pi bonds and rings within a molecule.
470 Benzene, toluene, and similar aromatics have $DBE = 4$, naphthalene = 7 and monoterpenes = 3.
471 DBE can be used as an indicator of sources when considering HOM in bulk. Saturation mass
472 concentration as calculated by equation 4 can help describe capacity of a molecule to both condense
473 onto newly formed particles and participate in nucleation. Figure 8 shows concentrations of HOMs

474 and other oxygenated organic molecules binned to the nearest integer $\text{Log}_{10}(C^*)(300\text{ K})$, coloured
475 by DBE. Mean ion signals per carbon number are shown in Figure S7. Most measured molecules
476 fall into the SVOC class ($0.3 < C^*(300\text{ K}) < 300\ \mu\text{g m}^{-3}$) which will mostly exist in equilibrium
477 between gas and particle phase. Highest SVOC concentrations arise from fingerprint molecules for
478 isoprene oxidation under high NO_x concentrations ($\text{C}_5\text{H}_{10}\text{N}_2\text{O}_8$) (Brean et al., 2020), and oxidation
479 of small alkylbenzenes ($\text{C}_7\text{H}_8\text{O}_5$, $\text{C}_8\text{H}_{10}\text{O}_5$). LVOC and ELVOC ($3 \cdot 10^{-5} < C^* < 0.3\ \mu\text{g m}^{-3}$ and $3 \cdot 10^{-9}$
480 $< C^*(300\text{ K}) < 3 \cdot 10^{-5}\ \mu\text{g m}^{-3}$ respectively) have a greater contribution from molecules with higher
481 DBE, i.e., $\text{C}_{10}\text{H}_{10}\text{O}_8$ arising most likely from PAH oxidation (Molteni et al., 2018), and $\text{C}_{10}\text{H}_{15}\text{O}_7\text{N}$,
482 a common molecule arising from monoterpene oxidation in the presence of NO_x . The contribution
483 of molecules with carbon number ≤ 9 to these LVOC is modest, and ELVOCs are entirely
484 comprised of molecules with carbon numbers ≥ 10 , and is dominated by DBEs of 8 and 4,
485 attributable to PAH and monoterpene oxidation respectively. No molecules classed as ultra-low
486 volatility organic compounds (ULVOC, $C^*(300\text{ K}) < 3 \cdot 10^{-9}\ \mu\text{g m}^{-3}$) were observed in our data, and
487 thus any pure HOM nucleation is unlikely.

488

489 **3.3.2 HOMs and NPF**

490 As shown in Figure 3, an elevated HOM concentration appears to be a necessary condition for particle
491 growth past 10 nm during NPF events. These days are associated with elevated temperatures, solar
492 radiation, higher ozone, and lower $\text{NO}:\text{NO}_2$ ratio. HIO_3 is also significantly higher on burst-event
493 days. A recent study in a remote environment reports growth rates matching condensation rates
494 without accounting for aqueous phase chemistry (Mohr et al., 2019). From 2D-VBS volatility
495 calculations discussed in the previous section, it is shown that LVOC and ELVOC measured in
496 Barcelona plausibly arise from the oxidation of aromatics (particularly PAHs in the case of ELVOC)
497 and monoterpenes. Calculated growth rates according to the method of Nieminen et al. (2010) are
498 presented in Figure S8 for both $\text{GR}_{1.9-5}$ and GR_{5-20} . Best agreement for GR_{5-20} is when condensation
499 of SVOC, LVOC, ELVOC, MSA, HIO_3 and H_2SO_4 is considered, and best agreement for $\text{GR}_{1.9-5}$ is

500 seen for condensation of all these except SVOC. The uncertainties in this method are large, and
501 assumptions of irreversible condensation of SVOC onto particles of 5 nm likely lead to
502 overestimations; however, these results indicate an essential role of the condensation of organic
503 compounds to produce high growth rates observed in urban environments.

504

505 Figure 9 shows three mass-defect plots for a non-event period, full-event period, and burst-event
506 period. The non-event day included in Figure 8 was characterised by lower solar radiation and
507 temperatures than average, so lower signals for oxygenated species are seen due to weaker
508 photochemistry (i.e., OH concentration), and slower autoxidation due to slower H-shift reactions
509 (Frege et al., 2018; Quéléver et al., 2019; Stolzenburg et al., 2018). The full-event day sees
510 enhancements to smaller OVOCs and HOMs compared to the non-event day, especially around
511 150-200 m/Q, which contains peaks corresponding to dicarboxylic acids and isoprene oxidation
512 products. Some of the largest peaks in the mass spectra correspond to formulae seen arising from
513 the enhanced OH oxidation of alkylbenzenes (such as $C_7H_7NO_6$) (Molteni et al., 2018; Wang et al.,
514 2017). Larger HOMs see a less significant enhancement to smaller alkylbenzene derived HOMs.
515 The presence of larger, unidentified HOMs >400 m/Q is enhanced during full-events, these peaks
516 will comprise the largest compounds, most likely of class ELVOC, arising from the oxidation of
517 large VOCs, or RO_2 - RO_2 accretion reactions, and thus, we likely underpredict ELVOC
518 concentrations and resultant impacts on particle growth in Figure S8. These unidentified peaks
519 >400 m/Q are both more numerous and larger during full-event periods, with a factor of two
520 difference in total peak area. The burst-event day has significantly lower concentrations of OVOCs
521 and HOMs, and to a lesser degree, their nitrogen containing counterparts (N-OVOCs and N-
522 HOMs), with significantly fewer compounds >400 m/Q. The most significant difference between
523 full and burst-event days is in the SVOCs, accounting for a factor of two difference in
524 concentration. The sulphur containing acids all have similar peak areas to the full-event day. These
525 elevations to condensable OVOCs and HOMs on particle formation days with growth are consistent

526 with particle composition data as measured by ACSM (Figure S9). Particle composition on full-
527 event days shows an elevation to organic mass concentration in the late evening and night around
528 when new particles from NPF will reach sizes detectable by the ACSM (~75 nm, Ng et al., 2011).
529 Organic mass between 16:00 and 23:00 is $3.5 \mu\text{g m}^{-3}$ on burst-event days, versus $7.8 \mu\text{g m}^{-3}$ on full-
530 event days.

531

532 **4. CONCLUSIONS**

533 We show new particle formation rates in Barcelona are linearly dependent upon the sulphuric acid
534 concentrations, and while formation rates far exceed that of $\text{H}_2\text{SO}_4\text{-BioOxOrg-H}_2\text{O}$ nucleation, they
535 fall short of those of $\text{H}_2\text{SO}_4\text{-DMA-H}_2\text{O}$ nucleation at 278 K, as does the sulphuric acid
536 dimer:monomer ratio, possibly explained by cluster evaporation due to high temperatures in
537 summertime Barcelona (303 K during events), and limited pools of gas-phase amines. These results
538 are similar to reports of nucleation rates in rural Germany (Kürten et al., 2016). As no higher-order
539 clusters were directly measured, we cannot determine nucleation mechanisms with certainty, and an
540 involvement of HOMs in nucleation is plausible.

541

542 High concentrations of OVOCs and HOMs were measured by CI-APi-ToF. Of these, the SVOC
543 arose from mostly isoprene and alkylbenzene oxidation, whereas LVOC and ELVOC arose from
544 alkylbenzene, monoterpene and PAH oxidation together, with a dependence of their concentration
545 on temperature. Concentrations of species associated with coastal and oceanic sources such as MSA
546 and HIO_3 were low. High HOM concentrations are seen to be a necessary condition for new particle
547 growth past 10 nm, with the most significant difference between days with and without particle
548 growth being SVOC concentrations (factor of 2 difference), while modelled growth rates from
549 condensation of these organic compounds, alongside H_2SO_4 , MSA and HIO_3 were shown to match
550 growth rates within measurement error. Thus, oxidation of traffic derived alkylbenzenes and PAHs,

551 and to a lesser degree, isoprene and monoterpene emissions is a significant determinant of new
552 particle growth in this environment.

553

554 These results are consistent with extensive chamber and flow tube studies on particle formation
555 from sulphuric acid, amines and HOMs, and further, nucleation rates relative to sulphuric acid are
556 similar to many tropospheric observations. Barcelona is representative of many Mediterranean
557 urban environments, with moderate pollution, influence of shipping emissions, and high insolation,
558 and the present study reveals the complexity of NPF mechanisms in these environments.

559

560 **DATA AVAILABILITY**

561 Data supporting this publication are openly available from the UBIRA eData repository at
562 <https://doi.org/10.25500/edata.bham.00000434>

563

564 **AUTHOR CONTRIBUTIONS**

565 RMH and XQ conceived the study, JB and DCSB carried out the CI-APi-TOF and related
566 measurements with assistance from AA and MCM. The VOC measurements were proposed by NM
567 and collected by BT-R. JB wrote the first draft of the manuscript which was enhanced by
568 contributions from the co-authors.

569

570 **COMPETING INTERESTS**

571 The authors have no conflict of interests.

572 **ACKNOWLEDGEMENTS**

573 Financial assistance from the Spanish Ministry of Science, Innovation and Universities and
574 Competitiveness and FEDER funds under the project HOUSE (CGL2016-78594-R), and by the
575 Generalitat de Catalunya (AGAUR 2017 SGR41) is gratefully acknowledged. MCM acknowledges

576 the Ramón y Cajal Fellowship awarded by the Spanish Ministry. Financial support of the UK
577 scientists by the Natural Environment Research Council through the National Centre for Atmospheric
578 Science is also acknowledged (R8/H12/83/011).

579

580 **REFERENCES**

581

582 Ábalos, M., Bayona, J. M. and Ventura, F.: Development of a solid-phase microextraction GC-NPD
583 procedure for the determination of free volatile amines in wastewater and sewage-polluted waters,
584 *Anal. Chem.*, 71(16), 3531–3537, doi:10.1021/ac990197h, 1999.

585

586 Almeida, J., Schobesberger, S., Kürten, A., Ortega, I. K., Kupiainen-Määttä, O., Praplan, A. P.,
587 Adamov, A., Amorim, A., Bianchi, F., Breitenlechner, M., David, A., Dommen, J., Donahue, N. M.,
588 Downard, A., Dunne, E., Duplissy, J., Ehrhart, S., Flagan, R. C., Franchin, A., Guida, R., Hakala, J.,
589 Hansel, A., Heinritzi, M., Henschel, H., Jokinen, T., Junninen, H., Kajos, M., Kangasluoma, J.,
590 Keskinen, H., Kupc, A., Kurtén, T., Kvashin, A. N., Laaksonen, A., Lehtipalo, K., Leiminger, M.,
591 Leppä, J., Loukonen, V., Makhmutov, V., Mathot, S., McGrath, M. J., Nieminen, T., Olenius, T.,
592 Onnela, A., Petäjä, T., Riccobono, F., Riipinen, I., Rissanen, M., Rondo, L., Ruuskanen, T., Santos,
593 F. D., Sarnela, N., Schallhart, S., Schnitzhofer, R., Seinfeld, J. H., Simon, M., Sipilä, M., Stozhkov,
594 Y., Stratmann, F., Tomé, A., Tröstl, J., Tsagkogeorgas, G., Vaattovaara, P., Viisanen, Y., Virtanen,
595 A., Vrtala, A., Wagner, P. E., Weingartner, E., Wex, H., Williamson, C., Wimmer, D., Ye, P., Yli-
596 Juuti, T., Carslaw, K. S., Kulmala, M., Curtius, J., Baltensperger, U., Worsnop, D. R., Vehkamäki,
597 H. and Kirkby, J.: Molecular understanding of sulphuric acid-amine particle nucleation in the
598 atmosphere, *Nature*, 502(7471), 359–363, doi:10.1038/nature12663, 2013.

599

600 Bianchi, F., Tröstl, J., Junninen, H., Frege, C., Henne, S., Hoyle, C. R., Molteni, U., Herrmann, E.,
601 Bukowiecki, N., Chen, X., Duplissy, J., Gysel, M., Hutterli, M., Kangasluoma, J., Kontkanen, J.,
602 Manninen, H. E., Münch, S., Peräkylä, O., Petäjä, T., Rondo, L., Williamson, C., Weingartner, E.,
603 Worsnop, D. R., Kulmala, M., Dommen, J. and Baltensperger, U.: New particle formation in the free
604 troposphere : A question of chemistry and timing, *Science*, 5456(May), 1–11, 2016.

605

606 Bianchi, F., Garmash, O., He, X., Yan, C., Iyer, S., Rosendahl, I., Xu, Z., Rissanen, M. P., Riva, M.,
607 Taipale, R., Sarnela, N., Petäjä, T., Worsnop, D. R., Kulmala, M., Ehn, M. and Junninen, H.: The role
608 of highly oxygenated molecules (HOMs) in determining the composition of ambient ions in the boreal
609 forest, *Atmos. Chem. Phys.*, 17(22), 13819–13831, doi:10.5194/acp-17-13819-2017, 2017.

610

611 Bianchi, F., Kurtén, T., Riva, M., Mohr, C., Rissanen, M. P., Roldin, P., Berndt, T., Crouse, J. D.,
612 Wennberg, P. O., Mentel, T. F., Wildt, J., Junninen, H., Jokinen, T., Kulmala, M., Worsnop, D. R.,
613 Thornton, J. A., Donahue, N., Kjaergaard, H. G. and Ehn, M.: Highly Oxygenated Organic Molecules
614 (HOM) from Gas-Phase Autoxidation Involving Peroxy Radicals: A Key Contributor to Atmospheric
615 Aerosol, *Chem. Rev.*, 2019.

616

617 Bousiotis, D., Dall'osto, M., Beddows, D. C. S., Pope, F. D. and Harrison, R. M.: Analysis of new
618 particle formation (NPF) events at nearby rural, urban background and urban roadside sites, *Atmos.*
619 *Chem. Phys.*, 19, 5679–5694, doi:10.5194/acp-19-5679-2019, 2019.

620

621 Brean, J., Harrison, R. M., Shi, Z., Beddows, D. C. S., Acton, W. J. F., Hewitt, C. N., Squires, F. A.,
622 and Lee, J.: Observations of highly oxidized molecules and particle nucleation in the atmosphere of
623 Beijing, *Atmos. Chem. Phys.*, 19, 14933–14947, <https://doi.org/10.5194/acp-19-14933-2019>, 2019.

624 Brines, M., Dall'Osto, M., Beddows, D. C. S., Harrison, R. M., and Querol, X.: Simplifying aerosol
625 size distributions modes simultaneously detected at four monitoring sites during SAPUSS, *Atmos.*
626 *Chem. Phys.*, 14, 2973–2986, <https://doi.org/10.5194/acp-14-2973-2014>, 2014.

627

628 Brines, M., Dall'Osto, M., Beddows, D. C. S., Harrison, R. M., Gómez-Moreno, F., Núñez, L.,
629 Artíñano, B., Costabile, F., Gobbi, G. P., Salimi, F., Morawska, L., Sioutas, C., and Querol, X.:
630 Traffic and nucleation events as main sources of ultrafine particles in high-insolation developed world
631 cities, *Atmos. Chem. Phys.*, 15, 5929–5945, <https://doi.org/10.5194/acp-15-5929-2015>, 2015.

632
633 Cadle, S. H. and Mulawa, P. A.: Low-molecular-weight aliphatic amines in exhaust from catalyst-
634 equipped cars, *Environ. Sci. Technol.*, 14(6), 718–723, doi:10.1021/es60166a011, 1980.
635
636 Carnerero, C., Pérez, N., Petäjä, T., Laurila, T. M., Ahonen, L. R., Kontkanen, J., Ahn, K. H.,
637 Alastuey, A. and Querol, X.: Relating high ozone, ultrafine particles, and new particle formation
638 episodes using cluster analysis, *Atmos. Environ. X*, 4(May), 1–20, doi:10.1016/j.aeaoa.2019.100051,
639 2019.
640
641 Cohen, A. J., Brauer, M., Burnett, R., Anderson, H. R., Frostad, J., Estep, K., Balakrishnan, K.,
642 Brunekreef, B., Dandona, L., Dandona, R., Feigin, V., Freedman, G., Hubbell, B., Jobling, A., Kan,
643 H., Knibbs, L., Liu, Y., Martin, R., Morawska, L., Pope, C. A., Shin, H., Straif, K., Shaddick, G.,
644 Thomas, M., van Dingenen, R., van Donkelaar, A., Vos, T., Murray, C. J. L. and Forouzanfar, M. H.:
645 Estimates and 25-year trends of the global burden of disease attributable to ambient air pollution: an
646 analysis of data from the Global Burden of Diseases Study 2015, *Lancet*, 389(10082), 1907–1918,
647 doi:10.1016/S0140-6736(17)30505-6, 2017.
648
649 Cubison, M. J. and Jimenez, J. L.: Statistical precision of the intensities retrieved from constrained
650 fitting of overlapping peaks in high-resolution mass spectra, *Atmos. Meas. Tech.*, 8(6), 2333–2345,
651 doi:10.5194/amt-8-2333-2015, 2015.
652
653 Curtius, J., Froyd, K. D. and Lovejoy, E. R.: Cluster ion thermal decomposition (I): Experimental
654 kinetics study and ab initio calculations for $\text{HSO}_4^-(\text{H}_2\text{SO}_4)_x(\text{HNO}_3)_y$, *J. Phys. Chem. A*, 105(48),
655 10867–10873, doi:10.1021/jp0124950, 2001.
656
657 Dal Maso, M., Kulmala, M., Riipinen, I., Wagner, R., Hussein, T., Aalto, P. P. and Lehtinen, K. E.
658 J.: Formation and growth of fresh atmospheric aerosols: Eight years of aerosol size distribution data
659 from SMEAR II, Hyytiälä, Finland, *Boreal Environ. Res.*, 10(5), 323–336, 2005.
660
661 Dall’Osto, M., Querol, X., Alastuey, A., O’Dowd, C., Harrison, R. M., Wenger, J. and Gómez-
662 Moreno, F. J.: On the spatial distribution and evolution of ultrafine particles in Barcelona, *Atmos.*
663 *Chem. Phys.*, 13(2), 741–759, doi:10.5194/acp-13-741-2013, 2013.
664
665 Donahue, N. M., Epstein, S. A., Pandis, S. N. and Robinson, A. L.: Atmospheric Chemistry and
666 Physics A two-dimensional volatility basis set: 1. organic-aerosol mixing thermodynamics, *Atmos.*
667 *Chem. Phys.*, 11, 3303–3318, doi:10.5194/acp-11-3303-2011, 2011.
668
669 Ehn, M., Thornton, J. A., Kleist, E., Sipilä, M., Junninen, H., Pullinen, I., Springer, M., Rubach, F.,
670 Tillmann, R., Lee, B., Lopez-Hilfiker, F., Andres, S., Acir, I.-H., Rissanen, M., Jokinen, T.,
671 Schobesberger, S., Kangasluoma, J., Kontkanen, J., Nieminen, T., Kurtén, T., Nielsen, L. B.,
672 Jørgensen, S., Kjaergaard, H. G., Canagaratna, M., Maso, M. D., Berndt, T., Petäjä, T., Wahner, A.,
673 Kerminen, V.-M., Kulmala, M., Worsnop, D. R., Wildt, J. and Mentel, T. F.: A large source of low-
674 volatility secondary organic aerosol, *Nature*, 506(7489), 476–479, doi:10.1038/nature13032, 2014.
675
676 Elm, J., Myllys, N. and Kurtén, T.: What is Required for Highly Oxidized Molecules to Form Clusters
677 with Sulphuric Acid?, *J. Phys. Chem. A*, 121(23), 4578–4587, doi:10.1021/acs.jpca.7b03759, 2017.
678
679 Frege, C., Ortega, I. K., Rissanen, M. P., Praplan, A. P., Steiner, G., Heinritzi, M., Ahonen, L.,
680 Amorim, A., Bernhammer, A. K., Bianchi, F., Brilke, S., Breitenlechner, M., Dada, L., Dias, A.,
681 Duplissy, J., Ehrhart, S., El-Haddad, I., Fischer, L., Fuchs, C., Garmash, O., Gonin, M., Hansel, A.,
682 Hoyle, C. R., Jokinen, T., Junninen, H., Kirkby, J., Kürten, A., Lehtipalo, K., Leiminger, M., Lee
683 Mauldin, R., Molteni, U., Nichman, L., Petäjä, T., Sarnela, N., Schobesberger, S., Simon, M., Sipilä,

684 M., Stolzenburg, D., Tomé, A., Vogel, A. L., Wagner, A. C., Wagner, R., Xiao, M., Yan, C., Ye, P.,
685 Curtius, J., Donahue, N. M., Flagan, R. C., Kulmala, M., Worsnop, D. R., Winkler, P., Dommen, J.
686 and Baltensperger, U.: Influence of temperature on the molecular composition of ions and charged
687 clusters during pure biogenic nucleation, *Atmos. Chem. Phys.*, 18(1), 65–79, doi:10.5194/acp-18-65-
688 2018, 2018.

689 Garmash, O., Rissanen, M. P., Pullinen, I., Schmitt, S., Kausiala, O., Tillmann, R., Zhao, D., Percival,
690 C., Bannan, T. J., Priestley, M., Hallquist, Å. M., Kleist, E., Kiendler-Scharr, A., Hallquist, M.,
691 Berndt, T., McFiggans, G., Wildt, J., Mentel, T. F., and Ehn, M.: Multi-generation OH oxidation as
692 a source for highly oxygenated organic molecules from aromatics, *Atmos. Chem. Phys.*, 20, 515–
693 537, doi:10.5194/acp-20-515-2020, 2020.

694 Ge, X., Wexler, A. S. and Clegg, S. L.: Atmospheric amines – Part I. A review, *Atmos. Environ.*,
695 45(3), 524–546, doi:10.1016/j.atmosenv.2010.10.012, 2011a.

696 Ge, X., Wexler, A. S. and Clegg, S. L.: Atmospheric amines – Part II. Thermodynamic properties and
697 gas/particle partitioning, *Atmos. Environ.*, 45(3), 561–577, doi:10.1016/j.atmosenv.2010.10.013,
698 2011b.

699 Graus, M., Müller, M. and Hansel, A.: High resolution PTR-TOF: Quantification and Formula
700 Confirmation of VOC in Real Time, *J. Am. Soc. Mass Spectrom.*, 21(6), 1037–1044,
701 doi:10.1016/j.jasms.2010.02.006, 2010.

702 Guo, S., Hu, M., Zamora, M. L., Peng, J., Shang, D., Zheng, J., Du, Z., Wu, Z., Shao, M., Zeng, L.,
703 Molina, M. J. and Zhang, R.: Elucidating severe urban haze formation in China., *Proc. Natl. Acad.*
704 *Sci. U. S. A.*, 111(49), 17373–8, doi:10.1073/pnas.1419604111, 2014.

705 Harrison, R. M., Rob Mackenzie, A., Xu, H., Alam, M. S., Nikolova, I., Zhong, J., Singh, A., Zeraati-
706 Rezaei, S., Stark, C., Beddows, D. C. S., Liang, Z., Xu, R. and Cai, X.: Diesel exhaust nanoparticles
707 and their behaviour in the atmosphere, *Proc. R. Soc. A Math. Phys. Eng. Sci.*, 474(2220),
708 doi:10.1098/rspa.2018.0492, 2018.

709 Henschel, S., Querol, X., Atkinson, R., Pandolfi, M., Zeka, A., Tertre, A. L., Analistis, A.,
710 Katsouyanni, K., Chanel, O., Pascal, M., Bouland, C., Haluza, D., Medina, S., and Goodman, P. G.:
711 Ambient air SO₂ patterns in 6 European cities, *Atmos. Environ.*, 79, 236–247,
712 doi:10.1016/j.atmosenv.2013.06.008, 2013.

713 Hirsikko, A., Nieminen, T., Gagné, S., Lehtipalo, K., Manninen, H. E., Ehn, M., Hörrak, U.,
714 Kerminen, V.-M., Laakso, L., McMurry, P. H., Mirme, A., Mirme, S., Petäjä, T., Tammet, H.,
715 Vakkari, V., Vana, M. and Kulmala, M.: Atmospheric ions and nucleation: a review of observations,
716 *Atmos. Chem. Phys.*, 11, 767–798, doi:10.5194/acp-11-767-2011, 2011.

717 Hutchinson, G. L., Mosier, A. R. and Andre, C. E.: Ammonia and Amine Emissions from a Large
718 Cattle Feedlot, *J. Environ. Qual.*, 11(2), 288–293, 1982.

719 Hyttinen, N., Kupiainen-Määttä, O., Rissanen, M. P., Muuronen, M., Ehn, M. and Kurtén, T.:
720 Modeling the Charging of Highly Oxidized Cyclohexene Ozonolysis Products Using Nitrate-Based
721 Chemical Ionization, *J. Phys. Chem. A*, 119(24), 6339–6345, doi:10.1021/acs.jpca.5b01818, 2015.

722 IPCC, 2013: Climate Change 2013: The Physical Science Basis. Contribution of Working Group I to
723 the Fifth Assessment Report of the Intergovernmental Panel on Climate Change, edited by V. B. and
724 P. M. M. Stocker, T.F., D. Qin, G.-K. Plattner, M. Tignor, S.K. Allen, J. Boschung, A. Nauels, Y.

735 Xia, Cambridge University Press, Cambridge., 2014.
736
737 Jen, C. N., Zhao, J., McMurry, P. H., and Hanson, D. R.: Chemical ionization of clusters formed from
738 sulfuric acid and dimethylamine or diamines, *Atmos. Chem. Phys.*, 16, 12513–12529,
739 doi:10.5194/acp-16-12513-2016, 2016.
740
741 Jokinen, T., Sipilä, M., Junninen, H., Ehn, M., Lönn, G., Hakala, J., Petäjä, T., Mauldin, R. L.,
742 Kulmala, M. and Worsnop, D. R.: Atmospheric sulphuric acid and neutral cluster measurements using
743 CI-API-TOF, *Atmos. Chem. Phys.*, 12(9), 4117–4125, doi:10.5194/acp-12-4117-2012, 2012.
744
745 Jokinen, T., Sipilä, M., Kontkanen, J., Vakkari, V., Tisler, P., Duplissy, E.-M., Junninen, H.,
746 Kangasluoma, J., Manninen, H. E., Petäjä, T., Kulmala, M., Worsnop, D. R., Kirkby, J., Virkkula, A.
747 and Kerminen, V.-M.: Ion-induced sulphuric acid–ammonia nucleation drives particle formation in
748 coastal Antarctica, *Sci. Adv.*, 4(11), eaat9744, doi:10.1126/sciadv.aat9744, 2018.
749
750 Junninen, H., Ehn, M., Petäjä, T., Luosujärvi, L., Kotiaho, T., Kostianen, R., Rohner, U., Gonin, M.,
751 Fuhrer, K., Kulmala, M. and Worsnop, D. R.: A high-resolution mass spectrometer to measure
752 atmospheric ion composition, *Atmos. Meas. Tech.*, 3(4), 1039–1053, doi:10.5194/amt-3-1039-2010,
753 2010.
754
755 Kerminen, V. M., Chen, X., Vakkari, V., Petäjä, T., Kulmala, M. and Bianchi, F.: Atmospheric new
756 particle formation and growth: Review of field observations, *Environ. Res. Lett.*, 13(10),
757 doi:10.1088/1748-9326/aadf3c, 2018.
758
759 Kirkby, J., Curtius, J., Almeida, J., Dunne, E., Duplissy, J., Ehrhart, S., Franchin, A., Gagné, S., Ickes,
760 L., Kürten, A., Kupc, A., Metzger, A., Riccobono, F., Rondo, L., Schobesberger, S., Tsagkogeorgas,
761 G., Wimmer, D., Amorim, A., Bianchi, F., Breitenlechner, M., David, A., Dommen, J., Downard, A.,
762 Ehn, M., Flagan, R. C., Haider, S., Hansel, A., Hauser, D., Jud, W., Junninen, H., Kreissl, F., Kvashin,
763 A., Laaksonen, A., Lehtipalo, K., Lima, J., Lovejoy, E. R., Makhmutov, V., Mathot, S., Mikkilä, J.,
764 Minginette, P., Mogo, S., Nieminen, T., Onnela, A., Pereira, P., Petäjä, T., Schnitzhofer, R., Seinfeld,
765 J. H., Sipilä, M., Stozhkov, Y., Stratmann, F., Tomé, A., Vanhanen, J., Viisanen, Y., Vrtala, A.,
766 Wagner, P. E., Walther, H., Weingartner, E., Wex, H., Winkler, P. M., Carslaw, K. S., Worsnop, D.
767 R., Baltensperger, U. and Kulmala, M.: Role of sulphuric acid, ammonia and galactic cosmic rays in
768 atmospheric aerosol nucleation, *Nature*, 476(7361), 429–435, doi:10.1038/nature10343, 2011.
769
770 Kirkby, J., Duplissy, J., Sengupta, K., Frege, C., Gordon, H., Williamson, C., Heinritzi, M., Simon,
771 M., Yan, C., Almeida, J., Trostl, J., Nieminen, T., Ortega, I. K., Wagner, R., Adamov, A., Amorim,
772 A., Bernhammer, A. K., Bianchi, F., Breitenlechner, M., Brilke, S., Chen, X., Craven, J., Dias, A.,
773 Ehrhart, S., Flagan, R. C., Franchin, A., Fuchs, C., Guida, R., Hakala, J., Hoyle, C. R., Jokinen, T.,
774 Junninen, H., Kangasluoma, J., Kim, J., Krapf, M., Kürten, A., Laaksonen, A., Lehtipalo, K.,
775 Makhmutov, V., Mathot, S., Molteni, U., Onnela, A., Perakyla, O., Piel, F., Petaja, T., Praplan, A. P.,
776 Pringle, K., Rap, A., Richards, N. A. D., Riipinen, I., Rissanen, M. P., Rondo, L., Sarnela, N.,
777 Schobesberger, S., Scott, C. E., Seinfeld, J. H., Sipilä, M., Steiner, G., Stozhkov, Y., Stratmann, F.,
778 Tomé, A., Virtanen, A., Vogel, A. L., Wagner, A. C., Wagner, P. E., Weingartner, E., Wimmer, D.,
779 Winkler, P. M., Ye, P., Zhang, X., Hansel, A., Dommen, J., Donahue, N. M., Worsnop, D. R.,
780 Baltensperger, U., Kulmala, M., Carslaw, K. S. and Curtius, J.: Ion-induced nucleation of pure
781 biogenic particles, *Nature*, 533(7604), 521–526, doi:10.1038/nature17953, 2016.
782
783 Kuang, C., McMurry, P. H., McCormick, A. V. and Eisele, F. L.: Dependence of nucleation rates on
784 sulfuric acid vapor concentration in diverse atmospheric locations, *J. Geophys. Res. Atmos.*, 113(10),
785 1–9, doi:10.1029/2007JD009253, 2008.
786

787 Kulmala, M., Dal Maso, M., Mäkelä, J. M., Pirjola, L., Väkevä, M., Aalto, P., Miikkulainen, P.,
788 Hämeri, K. and O'Dowd, C. D.: On the formation, growth and composition of nucleation mode
789 particles, *Tellus, Ser. B Chem. Phys. Meteorol.*, 53(4), 479–490, doi:10.1034/j.1600-0889.2001.d01-
790 33.x, 2001.

791
792 Kulmala, M., Petäjä, T., Nieminen, T., Sipilä, M., Manninen, H. E., Lehtipalo, K., Dal Maso, M.,
793 Aalto, P. P., Junninen, H., Paasonen, P., Riipinen, I., Lehtinen, K. E. J., Laaksonen, A. and Kerminen,
794 V.-M.: Measurement of the nucleation of atmospheric aerosol particles, *Nat. Protoc.*, 7(9), 1651–
795 1667, doi:10.1038/nprot.2012.091, 2012.

796
797 Kulmala, M., Kerminen, V. M., Petäjä, T., Ding, A. J. and Wang, L.: Atmospheric gas-to-particle
798 conversion: Why NPF events are observed in megacities?, *Faraday Discuss.*, 200, 271–288,
799 doi:10.1039/c6fd00257a, 2017.

800
801 Kürten, A., Jokinen, T., Simon, M., Sipilä, M., Sarnela, N., Junninen, H., Adamov, A., Almeida, J.,
802 Amorim, A., Bianchi, F., Breitenlechner, M., Dommen, J., Donahue, N. M., Duplissy, J., Ehrhart, S.,
803 Flagan, R. C., Franchin, A., Hakala, J., Hansel, A., Heinritzi, M., Hutterli, M., Kangasluoma, J.,
804 Kirkby, J., Laaksonen, A., Lehtipalo, K., Leiminger, M., Makhmutov, V., Mathot, S., Onnela, A.,
805 Petäjä, T., Praplan, A. P., Riccobono, F., Rissanen, M. P., Rondo, L., Schobesberger, S., Seinfeld, J.
806 H., Steiner, G., Tomé, A., Tröstl, J., Winkler, P. M., Williamson, C., Wimmer, D., Ye, P.,
807 Baltensperger, U., Carslaw, K. S., Kulmala, M., Worsnop, D. R. and Curtius, J.: Neutral molecular
808 cluster formation of sulfuric acid–dimethylamine observed in real time under atmospheric conditions,
809 *Proc. Natl. Acad. Sci.*, 111(42), 15019–15024, doi:10.1073/pnas.1404853111, 2014.

810
811 Kürten, A., Münch, S., Rondo, L., Bianchi, F., Duplissy, J., Jokinen, T., Junninen, H., Sarnela, N.,
812 Schobesberger, S., Simon, M., Sipilä, M., Almeida, J., Amorim, A., Dommen, J., Donahue, N. M.,
813 Dunne, E. M., Flagan, R. C., Franchin, A., Kirkby, J., Kupc, A., Makhmutov, V., Petäjä, T., Praplan,
814 A. P., Riccobono, F., Steiner, G., Tomé, A., Tsagkogeorgas, G., Wagner, P. E., Wimmer, D.,
815 Baltensperger, U., Kulmala, M., Worsnop, D. R. and Curtius, J.: Thermodynamics of the formation
816 of sulfuric acid dimers in the binary (H₂SO₄-H₂O) and ternary (H₂SO₄-H₂O-NH₃) system, *Atmos.*
817 *Chem. Phys.*, 15(18), 10701–10721, doi:10.5194/acp-15-10701-2015, 2015.

818
819 Kürten, A., Bergen, A., Heinritzi, M., Leiminger, M., Lorenz, V., Piel, F., Simon, M., Sitals, R.,
820 Wagner, A. C. and Curtius, J.: Observation of new particle formation and measurement of sulphuric
821 acid, ammonia, amines and highly oxidized organic molecules at a rural site in central Germany,
822 *Atmos. Chem. Phys.*, 16(19), 12793–12813, doi:10.5194/acp-16-12793-2016, 2016.

823
824 Kürten, A., Li, C., Bianchi, F., Curtius, J., Dias, A., Donahue, N. M., Duplissy, J., Flagan, R. C.,
825 Hakala, J., Jokinen, T., Kirkby, J., Kulmala, M., Laaksonen, A., Lehtipalo, K., Makhmutov, V.,
826 Onnela, A., Rissanen, M. P., Simon, M., Sipilä, M., Stozhkov, Y., Tröstl, J., Ye, P. and McMurry, P.
827 H.: New particle formation in the sulfuric acid-dimethylamine-water system: Reevaluation of
828 CLOUD chamber measurements and comparison to an aerosol nucleation and growth model, *Atmos.*
829 *Chem. Phys.*, 18(2), 845–863, doi:10.5194/acp-18-845-2018, 2018.

830
831 Kurtén, T., Noppel, M., Vehkamäki, H., Salonen, M. and Kulmala, M.: Quantum chemical studies of
832 hydrate formation of H₂SO₄ and HSO₄⁻, *Boreal Environ. Res.*, 12(3), 431–453, 2007.

833
834 Kurtén, T., Loukonen, V., Vehkamäki, H. and Kulmala, M.: Amines are likely to enhance neutral and
835 ion-induced sulphuric acid-water nucleation in the atmosphere more effectively than ammonia,
836 *Atmos. Chem. Phys.*, 8(14), 4095–4103, doi:10.5194/acp-8-4095-2008, 2008.

837 Lee, S. H., Gordon, H., Yu, H., Lehtipalo, K., Haley, R., Li, Y. and Zhang, R.: New Particle Formation

838 in the Atmosphere: From Molecular Clusters to Global Climate, *J. Geophys. Res. Atmos.*,
839 doi:10.1029/2018JD029356, 2019.

840

841 Lehtinen, K. E. J., Dal Maso, M., Kulmala, M. and Kerminen, V. M.: Estimating nucleation rates
842 from apparent particle formation rates and vice versa: Revised formulation of the Kerminen-Kulmala
843 equation, *J. Aerosol Sci.*, 38(9), 988–994, doi:10.1016/j.jaerosci.2007.06.009, 2007.

844

845 Lehtinen, K. E. J., Dal Maso, M., Kulmala, M. and Kerminen, V. M.: Estimating nucleation rates
846 from apparent particle formation rates and vice versa: Revised formulation of the Kerminen-Kulmala
847 equation, *J. Aerosol Sci.*, 38(9), 988–994, doi:10.1016/j.jaerosci.2007.06.009, 2007.

848

849 Lehtipalo, K., Yan, C., Dada, L., Bianchi, F., Xiao, M., Wagner, R., Stolzenburg, D., Ahonen, L. R.,
850 Amorim, A., Baccarini, A., Bauer, P. S., Baumgartner, B., Bergen, A., Bernhammer, A.-K.,
851 Breitenlechner, M., Brilke, S., Buchholz, A., Mazon, S. B., Chen, D., Chen, X., Dias, A., Dommen,
852 J., Draper, D. C., Duplissy, J., Ehn, M., Finkenzeller, H., Fischer, L., Frege, C., Fuchs, C., Garmash,
853 O., Gordon, H., Hakala, J., He, X., Heikkinen, L., Heinritzi, M., Helm, J. C., Hofbauer, V., Hoyle, C.
854 R., Jokinen, T., Kangasluoma, J., Kerminen, V.-M., Kim, C., Kirkby, J., Kontkanen, J., Kürten, A.,
855 Lawler, M. J., Mai, H., Mathot, S., Mauldin, R. L., Molteni, U., Nichman, L., Nie, W., Nieminen, T.,
856 Ojdanic, A., Onnela, A., Passananti, M., Petäjä, T., Piel, F., Pospisilova, V., Quéléver, L. L. J.,
857 Rissanen, M. P., Rose, C., Sarnela, N., Schallhart, S., Schuchmann, S., Sengupta, K., Simon, M.,
858 Sipilä, M., Tauber, C., Tomé, A., Tröstl, J., Väisänen, O., Vogel, A. L., Volkamer, R., Wagner, A.
859 C., Wang, M., Weitz, L., Wimmer, D., Ye, P., Ylisirniö, A., Zha, Q., Carslaw, K. S., Curtius, J.,
860 Donahue, N. M., Flagan, R. C., Hansel, A., Riipinen, I., Virtanen, A., Winkler, P. M., Baltensperger,
861 U., Kulmala, M. and Worsnop, D. R.: Multicomponent new particle formation from sulphuric acid,
862 ammonia, and biogenic vapors, *Sci. Adv.*, 4(12), eaau5363, doi:10.1126/sciadv.aau5363, 2018.

863

864 Massoli, P., Stark, H., Canagaratna, M. R., Krechmer, J. E., Xu, L., Ng, N. L., Mauldin, R. L., Yan,
865 C., Kimmel, J., Misztal, P. K., Jimenez, J. L., Jayne, J. T. and Worsnop, D. R.: Ambient
866 Measurements of Highly Oxidized Gas-Phase Molecules during the Southern Oxidant and Aerosol
867 Study (SOAS) 2013, *ACS Earth Sp. Chem.*, 2(7), 653–672,
868 doi:10.1021/acsearthspacechem.8b00028, 2018.

869

870 Mikkonen, S., Romakkaniemi, S., Smith, J. N., Korhonen, H., Petäjä, T., Plass-Duelmer, C., Boy, M.,
871 McMurry, P. H., Lehtinen, K. E. J., Joutsensaari, J., Hamed, A., Mauldin, R. L., Birmili, W., Spindler,
872 G., Arnold, F., Kulmala, M. and Laaksonen, A.: A statistical proxy for sulphuric acid concentration,
873 *Atmos. Chem. Phys.*, 11(21), 11319–11334, doi:10.5194/acp-11-11319-2011, 2011.

874

875 Millán, M.: Extreme hydrometeorological events and climate change predictions in Europe, *J.*
876 *Hydrol.*, 518(PB), 206–224, doi:10.1016/j.jhydrol.2013.12.041, 2014.

877

878 Miller, M. R., Raftis, J. B., Langrish, J. P., McLean, S. G., Samutrtai, P., Connell, S. P., Wilson, S.,
879 Vesey, A. T., Fokkens, P. H. B., Boere, A. J. F., Krystek, P., Campbell, C. J., Hadoke, P. W. F.,
880 Donaldson, K., Cassee, F. R., Newby, D. E., Duffin, R. and Mills, N. L.: Inhaled Nanoparticles
881 Accumulate at Sites of Vascular Disease, *ACS Nano*, 11(5), 4542–4552,
882 doi:10.1021/acsnano.6b08551, 2017.

883

884 Minguillón, M. C., Brines, M., Pérez, N., Reche, C., Pandol, M., Fonseca, A. S., Amato, F., Alastuey,
885 A., Lyasota, A., Codina, B., Lee, H., Eun, H., Ahn, K. and Querol, X.: New particle formation at
886 ground level and in the vertical column over the Barcelona area, 165, 118–130,
887 doi:10.1016/j.atmosres.2015.05.003, 2015.

888

889 Minguillón, M.C., Pérez, N., Marchand, N., Bertrand, A., Temime-Roussel, B., Agrios, K., Szidat,

890 S., van Drooge, B.L., Sylvestre, A., Alastuey, A., Reche, C., Ripoll, A., Marco, E., Grimalt, J.O.,
891 Querol, X.: Secondary organic aerosol origin in an urban environment. Influence of biogenic and fuel
892 combustion precursors. *Faraday Discuss.*, 189, 337-359, 2016.
893
894 Mohr, C., Thornton, J. A., Heitto, A., Lopez-Hilfiker, F. D., Lutz, A., Riipinen, I., Hong, J., Donahue,
895 N. M., Hallquist, M., Petäjä, T., Kulmala, M. and Yli-Juuti, T.: Molecular identification of organic
896 vapors driving atmospheric nanoparticle growth, *Nat. Commun.*, 10(1), 1–7, doi:10.1038/s41467-
897 019-12473-2, 2019.
898
899 Møller, K. H., Tram, C. M. and Kjaergaard, H. G.: Side-by-Side Comparison of Hydroperoxide and
900 Corresponding Alcohol as Hydrogen-Bond Donors, *J. Phys. Chem. A*, 121(15), 2951–2959,
901 doi:10.1021/acs.jpca.7b01323, 2017.
902
903 Molteni, U., Bianchi, F., Klein, F., El Haddad, I., Frege, C., Rossi, M. J., Dommen, J. and
904 Baltensperger, U.: Formation of highly oxygenated organic molecules from aromatic compounds,
905 *Atmos. Chem. Phys.*, 18(3), 1909–1921, doi:10.5194/acp-18-1909-2018, 2018.
906
907 Ng, N. L., Herndon, S. C., Trimborn, A., Canagaratna, M. R., Croteau, P. L., Onasch, T. B., Sueper,
908 D., Worsnop, D. R., Zhang, Q., Sun, Y. L. and Jayne, J. T.: An Aerosol Chemical Speciation Monitor
909 (ACSM) for routine monitoring of the composition and mass concentrations of ambient aerosol,
910 *Aerosol Sci. Technol.*, 45(7), 770–784, doi:10.1080/02786826.2011.560211, 2011.
911
912 Nieminen, T., Lehtinen, K. E. J., and Kulmala, M.: Sub-10 nm particle growth by vapor condensation
913 – effects of vapor molecule size and particle thermal speed, *Atmos. Chem. Phys.*, 10, 9773–9779,
914 doi:10.5194/acp-10-9773-2010, 2010
915
916 Olenius, T., Halonen, R., Kurtén, T., Henschel, H., Kupiainen-Määttä, O., Ortega, I. K., Jen, C. N.,
917 Vehkamäki, H. and Riipinen, I.: New particle formation from sulfuric acid and amines: Comparison
918 of monomethylamine, dimethylamine, and trimethylamine, *J. Geophys. Res.*, 122(13), 7103–7118,
919 doi:10.1002/2017JD026501, 2017.
920
921 Olin, M., Kuuluvainen, H., Aurela, M., Kalliokoski, J., Kuittinen, N., Isotalo, M., Timonen, H. J.,
922 Niemi, J. V., Rönkkö, T., and Dal Maso, M.: Traffic-originated nanocluster emission exceeds H₂SO₄-
923 driven photochemical new particle formation in an urban area, *Atmos. Chem. Phys.*, 20, 1–13,
924 <https://doi.org/10.5194/acp-20-1-2020>, 2020.
925
926 Ortega, I. K., Olenius, T., Kupiainen-Määttä, O., Loukonen, V., Kurtén, T., and Vehkamäki, H.:
927 Electrical charging changes the composition of sulfuric acid–ammonia/dimethylamine clusters,
928 *Atmos. Chem. Phys.*, 14, 7995–8007, <https://doi.org/10.5194/acp-14-7995-2014>, 2014.
929
930 Paasonen, P., Olenius, T., Kupiainen, O., Kurtén, T., Petäjä, T., Birmili, W., Hamed, A., Hu, M.,
931 Huey, L. G., Plass-Duelmer, C., Smith, J. N., Wiedensohler, A., Loukonen, V., McGrath, M. J.,
932 Ortega, I. K., Laaksonen, A., Vehkamäki, H. and Kulmala, M.: On the formation of sulphuric acid
933 – Amine clusters in varying atmospheric conditions and its influence on atmospheric new
934 particle formation, *Atmos. Chem. Phys.*, 12(19), 9113–9133, doi:10.5194/acp-12-9113-2012, 2012.
935
936 Pandolfi, M., Amato, F., Reche, C., Alastuey, A., Otjes, R. P., Blom, M. J. and Querol, X.: Summer
937 ammonia measurements in a densely populated Mediterranean city, *Atmos. Chem. Phys.*, 12(16),
938 7557–7575, doi:10.5194/acp-12-7557-2012, 2012.
939
940 Passananti, M., Zapadinsky, E., Zanca, T., Kangasluoma, J., Mylly, N., Rissanen, M. P., Kurtén, T.,
941 Ehn, M., Attoui, M. and Vehkamäki, H.: How well can we predict cluster fragmentation inside a mass

942 spectrometer?, *Chem. Commun.*, 55(42), 5946–5949, doi:10.1039/c9cc02896j, 2019.
943

944 Penner, J. E., Xu, L. and Wang, M.: Satellite methods underestimate indirect climate forcing by
945 aerosols., *Proc. Natl. Acad. Sci. U. S. A.*, 108(33), 13404–13408, doi:10.1073/pnas.1018526108,
946 2011.

947

948 Praske, E., Otkjær, R. V., Crouse, J. D., Hethcox, J. C., Stoltz, B. M., Kjaergaard, H. G. and
949 Wennberg, P. O.: Atmospheric autoxidation is increasingly important in urban and suburban North
950 America, *Proc. Natl. Acad. Sci.*, 115(1), 64–69, doi:10.1073/pnas.1715540115, 2018.
951

952 Quéléver, L. L. J., Kristensen, K., Normann Jensen, L., Rosati, B., Teiwes, R., Daellenbach, K. R.,
953 Peräkylä, O., Roldin, P., Bossi, R., Pedersen, H. B., Glasius, M., Bilde, M. and Ehn, M.: Effect of
954 temperature on the formation of highly oxygenated organic molecules (HOMs) from alpha-pinene
955 ozonolysis, *Atmos. Chem. Phys.*, 19, 7609–7625, doi:10.5194/acp-19-7609-2019, 2019.
956

957 Querol, X., Gangoiti, G., Mantilla, E., Alastuey, A., Minguillón, M. C., Amato, F., Reche, C., Viana,
958 M., Moreno, T., Karanasiou, A., Rivas, I., Pérez, N., Ripoll, A., Brines, M., Ealo, M., Pandolfi, M.,
959 Lee, H. K., Eun, H. R., Park, Y. H., Escudero, M., Beddows, D., Harrison, R. M., Bertrand, A.,
960 Marchand, N., Lyasota, A., Codina, B., Olid, M., Udina, M., Jiménez-Esteve, B., Jiménez-Esteve, B.
961 B., Alonso, L., Millán, M. and Ahn, K. H.: Phenomenology of high-ozone episodes in NE Spain,
962 *Atmos. Chem. Phys.*, 17(4), 2817–2838, doi:10.5194/acp-17-2817-2017, 2017.
963

964 Reche, C., Viana, M., Karanasiou, A., Cusack, M., Alastuey, A., Artiñano, B., Revuelta, M. A.,
965 López-Mahía, P., Blanco-Heras, G., Rodríguez, S., Sánchez de la Campa, A. M., Fernández-
966 Camacho, R., González-Castanedo, Y., Mantilla, E., Tang, Y. S. and Querol, X.: Urban NH₃ levels
967 and sources in six major Spanish cities, *Chemosphere*, 119, 769–777,
968 doi:10.1016/j.chemosphere.2014.07.097, 2015.
969

970 Riccobono, F., Schobesberger, S., Scott, C., Dommen, J., Ortega, I., Rondo, L., Almeida, J., Amorim,
971 A., Bianchi, F., Breitenlechner, M., David, A., Downard, A., Dunne, E., Duplissy, J., Ehrhart, S.,
972 Flagan, R., Franchin, A., Hansel, A., Junninen, H., Kajos, M., Keskinen, H., Kupc, A., Kürten, A.,
973 Kvashin, A., Laaksonen, A., Lehtipalo, K., Makhmutov, V., Mathot, S., Nieminen, T., Onnela, A.,
974 Petäjä, T., Praplan, A., Santos, F., Schallhart, S., Seinfeld, J., Sipilä, M., Van Spracklen, D., Stozhkov,
975 Y., Stratmann, F., Tomé, A., Tsagkogeorgas, G., Vaattovaara, P., Viisanen, Y., Vrtala, A., Wagner,
976 P., Weingartner, E., Wex, H., Wimmer, D., Carslaw, K., Curtius, J., Donahue, N., Kirkby, J.,
977 Kulmala, M., Worsnop, D. and Baltensperger, U.: Oxidation products of biogenic emissions
978 contribute to nucleation of atmospheric particles., *Science*, 344(6185), 717–721,
979 doi:10.1126/science.1243527, 2014.
980

981 Rissanen, M. P.: NO₂ Suppression of Autoxidation-Inhibition of Gas-Phase Highly Oxidized Dimer
982 Product Formation, *ACS Earth Sp. Chem.*, 2(11), 1211–1219,
983 doi:10.1021/acsearthspacechem.8b00123, 2018.
984

985 Rose, C., Zha, Q., Dada, L., Yan, C., Lehtipalo, K., Junninen, H., Mazon, S. B., Jokinen, T., Sarnela,
986 N., Sipilä, M., Petäjä, T., Kerminen, V.-M., Bianchi, F. and Kulmala, M.: Observations of biogenic
987 ion-induced cluster formation in the atmosphere, *Sci. Adv.*, 4(4), 5218, doi:10.1126/sciadv.aar5218,
988 2018.
989

990 Schervish, M. and Donahue, N. M.: Peroxy radical chemistry and the volatility basis set, *Atmos.*
991 *Chem. Phys.*, 20(2), 1183–1199, doi:10.5194/acp-20-1183-2020, 2020.
992

993 Schobesberger, S., Junninen, H., Bianchi, F., Lönn, G., Ehn, M., Lehtipalo, K., Dommen, J., Ehrhart,

994 S., Ortega, I. K., Franchin, A., Nieminen, T., Riccobono, F., Hutterli, M., Duplissy, J., Almeida, J.,
 995 Amorim, A., Breitenlechner, M., Downard, A. J., Dunne, E. M., Flagan, R. C., Kajos, M., Keskinen,
 996 H., Kirkby, J., Kupc, A., Kürten, A., Kurtén, T., Laaksonen, A., Mathot, S., Onnela, A., Praplan, A.
 997 P., Rondo, L., Santos, F. D., Schallhart, S., Schnitzhofer, R., Sipilä, M., Tomé, A., Tsagkogeorgas,
 998 G., Vehkamäki, H., Wimmer, D., Baltensperger, U., Carslaw, K. S., Curtius, J., Hansel, A., Petäjä,
 999 T., Kulmala, M., Donahue, N. M. and Worsnop, D. R.: Molecular understanding of atmospheric
 1000 particle formation from sulphuric acid and large oxidized organic molecules., *Proc. Natl. Acad. Sci.*
 1001 *U. S. A.*, 110(43), 17223–17228, doi:10.1073/pnas.1306973110, 2013.
 1002
 1003 Simon, M., Heinritzi, M., Herzog, S., Leiminger, M., Bianchi, F., Praplan, A., Dommen, J., Curtius,
 1004 J. and Kürten, A.: Detection of dimethylamine in the low pptv range using nitrate chemical ionization
 1005 atmospheric pressure interface time-of-flight (CI-API-TOF) mass spectrometry, *Atmos. Meas. Tech.*,
 1006 9(5), 2135–2145, doi:10.5194/amt-9-2135-2016, 2016.
 1007
 1008 Sipilä, M., Sarnela, N., Jokinen, T., Henschel, H., Junninen, H., Kontkanen, J., Richters, S.,
 1009 Kangasluoma, J., Franchin, A., Peräkylä, O., Rissanen, M. P., Ehn, M., Vehkamäki, H., Kürten, T.,
 1010 Berndt, T., Petäjä, T., Worsnop, D., Ceburnis, D., Kerminen, V. M., Kulmala, M. and O’Dowd, C.:
 1011 Molecular-scale evidence of aerosol particle formation via sequential addition of HIO₃, *Nature*,
 1012 537(7621), 532–534, doi:10.1038/nature19314, 2016.
 1013
 1014 Stolzenburg, D., Fischer, L., Vogel, A. L., Heinritzi, M., Schervish, M., Simon, M., Wagner, A. C.,
 1015 Dada, L., Ahonen, L. R., Amorim, A., Baccarini, A., Bauer, P. S., Baumgartner, B., Bergen, A.,
 1016 Bianchi, F., Breitenlechner, M., Brilke, S., Buenrostro Mazon, S., Chen, D., Dias, A., Draper, D. C.,
 1017 Duplissy, J., El Haddad, I., Finkenzeller, H., Frege, C., Fuchs, C., Garmash, O., Gordon, H., He, X.,
 1018 Helm, J., Hofbauer, V., Hoyle, C. R., Kim, C., Kirkby, J., Kontkanen, J., Kürten, A., Lampilahti, J.,
 1019 Lawler, M., Lehtipalo, K., Leiminger, M., Mai, H., Mathot, S., Mentler, B., Molteni, U., Nie, W.,
 1020 Nieminen, T., Nowak, J. B., Ojdanic, A., Onnela, A., Passananti, M., Petäjä, T., Quéléver, L. L. J.,
 1021 Rissanen, M. P., Sarnela, N., Schallhart, S., Tauber, C., Tomé, A., Wagner, R., Wang, M., Weitz, L.,
 1022 Wimmer, D., Xiao, M., Yan, C., Ye, P., Zha, Q., Baltensperger, U., Curtius, J., Dommen, J., Flagan,
 1023 R. C., Kulmala, M., Smith, J. N., Worsnop, D. R., Hansel, A., Donahue, N. M. and Winkler, P. M.:
 1024 Rapid growth of organic aerosol nanoparticles over a wide tropospheric temperature range,
 1025 *P. Natl. Acad. Sci. USA*, 115, 9122–9127, 2018.
 1026
 1027 Tröstl, J., Chuang, W. K., Gordon, H., Heinritzi, M., Yan, C., Molteni, U., Ahlm, L., Frege, C.,
 1028 Bianchi, F., Wagner, R., Simon, M., Lehtipalo, K., Williamson, C., Craven, J. S., Duplissy, J.,
 1029 Adamov, A., Almeida, J., Bernhammer, A. K., Breitenlechner, M., Brilke, S., Dias, A., Ehrhart, S.,
 1030 Flagan, R. C., Franchin, A., Fuchs, C., Guida, R., Gysel, M., Hansel, A., Hoyle, C. R., Jokinen, T.,
 1031 Junninen, H., Kangasluoma, J., Keskinen, H., Kim, J., Krapf, M., Kürten, A., Laaksonen, A., Lawler,
 1032 M., Leiminger, M., Mathot, S., Möhler, O., Nieminen, T., Onnela, A., Petäjä, T., Piel, F. M.,
 1033 Miettinen, P., Rissanen, M. P., Rondo, L., Sarnela, N., Schobesberger, S., Sengupta, K., Sipilä, M.,
 1034 Smith, J. N., Steiner, G., Tomé, A., Virtanen, A., Wagner, A. C., Weingartner, E., Wimmer, D.,
 1035 Winkler, P. M., Ye, P., Carslaw, K. S., Curtius, J., Dommen, J., Kirkby, J., Kulmala, M., Riipinen, I.,
 1036 Worsnop, D. R., Donahue, N. M. and Baltensperger, U.: The role of low-volatility organic compounds
 1037 in initial particle growth in the atmosphere, *Nature*, 533(7604), 527–531, doi:10.1038/nature18271,
 1038 2016.
 1039
 1040 Van Damme, M., Clarisse, L., Whitburn, S., Hadji-Lazarou, J., Hurtmans, D., Clerbaux, C. and
 1041 Coheur, P. F.: Industrial and agricultural ammonia point sources exposed, *Nature*, 564(7734), 99–
 1042 103, doi:10.1038/s41586-018-0747-1, 2018.
 1043
 1044 Wang, S., Wu, R., Berndt, T., Ehn, M. and Wang, L.: Formation of Highly Oxidized Radicals and
 1045 Multifunctional Products from the Atmospheric Oxidation of Alkylbenzenes, *Environ. Sci. Technol.*,

1046 51(15), 8442–8449, doi:10.1021/acs.est.7b02374, 2017.
1047
1048 Yan, C., Nie, W., Äijälä, M., Rissanen, M. P., Canagaratna, M. R., Massoli, P., Junninen, H., Jokinen,
1049 T., Sarnela, N., Häme, S. A. K., Schobesberger, S., Canonaco, F., Yao, L., Prévôt, A. S. H., Petäjä,
1050 T., Kulmala, M., Sipilä, M., Worsnop, D. R. and Ehn, M.: Source characterization of highly oxidized
1051 multifunctional compounds in a boreal forest environment using positive matrix factorization, *Atmos.*
1052 *Chem. Phys.*, 16(19), 12715–12731, doi:10.5194/acp-16-12715-2016, 2016.
1053
1054 Yan, C., Dada, L., Rose, C., Jokinen, T., Nie, W., Schobesberger, S., Junninen, H., Lehtipalo, K.,
1055 Sarnela, N., Makkonen, U., Garmash, O., Wang, Y., Zha, Q., Paasonen, P., Bianchi, F., Sipilä, M.,
1056 Ehn, M., Petäjä, T., Kerminen, V.-M., Worsnop, D. R., and Kulmala, M.: The role of H₂SO₄-NH₃
1057 anion clusters in ion-induced aerosol nucleation mechanisms in the boreal forest, *Atmos. Chem.*
1058 *Phys.*, 18, 13231–13243, <https://doi.org/10.5194/acp-18-13231-2018>, 2018.
1059
1060 Yan, C., Nie, W., Vogel, A. L., Dada, L., Lehtipalo, K., Stolzenburg, D., Wagner, R., Rissanen, M.
1061 P., Xiao, M., Ahonen, L., Fischer, L., Rose, C., Bianchi, F., Gordon, H., Simon, M., Heinritzi, M.,
1062 Garmash, O., Roldin, P., Dias, A., Ye, P., Hofbauer, V., Amorim, A., Bauer, P. S., Bergen, A.,
1063 Bernhammer, A.-K., Breitenlechner, M., Brilke, S., Buchholz, A., Mazon, S. B., Canagaratna, M. R.,
1064 Chen, X., Ding, A., Dommen, J., Draper, D. C., Duplissy, J., Frege, C., Heyn, C., Guida, R., Hakala,
1065 J., Heikkinen, L., Hoyle, C. R., Jokinen, T., Kangasluoma, J., Kirkby, J., Kontkanen, J., Kürten, A.,
1066 Lawler, M. J., Mai, H., Mathot, S., Mauldin, R. L., Molteni, U., Nichman, L., Nieminen, T., Nowak,
1067 J., Ojdanic, A., Onnela, A., Pajunoja, A., Petäjä, T., Piel, F., Quéléver, L. L. J., Sarnela, N., Schallhart,
1068 S., Sengupta, K., Sipilä, M., Tomé, A., Tröstl, J., Väisänen, O., Wagner, A. C., Ylisirniö, A., Zha, Q.,
1069 Baltensperger, U., Carslaw, K. S., Curtius, J., Flagan, R. C., Hansel, A., Riipinen, I., Smith, J. N.,
1070 Virtanen, A., Winkler, P. M., Donahue, N. M., Kerminen, V.-M., Kulmala, M., Ehn, M. and Worsnop,
1071 D. R.: Size-dependent influence of NO_x on the growth rates of organic aerosol particles, *Sci. Adv.*,
1072 6(22), eaay4945, doi:10.1126/sciadv.aay4945, 2020.
1073
1074 Yao, L., Garmash, O., Bianchi, F., Zheng, J., Yan, C., Kontkanen, J., Junninen, H., Mazon, S. B.,
1075 Ehn, M., Paasonen, P., Sipilä, M., Wang, M., Wang, X., Xiao, S., Chen, H., Lu, Y., Zhang, B., Wang,
1076 D., Fu, Q., Geng, F., Li, L., Wang, H., Qiao, L., Yang, X., Chen, J., Kerminen, V. M., Petäjä, T.,
1077 Worsnop, D. R., Kulmala, M. and Wang, L.: Atmospheric new particle formation from sulphuric acid
1078 and amines in a Chinese megacity, *Science*, 361(6399), 278–281, doi:10.1126/science.aao4839,
1079 2018.
1080
1081 Yli-Juuti, T., Pajunoja, A., Tikkanen, O. P., Buchholz, A., Faiola, C., Väisänen, O., Hao, L., Kari, E.,
1082 Peräkylä, O., Garmash, O., Shiraiwa, M., Ehn, M., Lehtinen, K. and Virtanen, A.: Factors controlling
1083 the evaporation of secondary organic aerosol from α -pinene ozonolysis, *Geophys. Res. Lett.*, 44(5),
1084 2562–2570, doi:10.1002/2016GL072364, 2017.
1085
1086 Yu, H., Zhou, L., Dai, L., Shen, W., Dai, W., Zheng, J., Ma, Y. and Chen, M.: Nucleation and growth
1087 of sub-3 nm particles in the polluted urban atmosphere of a megacity in China, *Atmos. Chem. Phys.*,
1088 16(4), 2641–2657, doi:10.5194/acp-16-2641-2016, 2016.
1089
1090 Zhang, R., Khalizov, A., Wang, L., Hu, M. and Xu, W.: Nucleation and growth of nanoparticles in
1091 the atmosphere, *Chem. Rev.*, 112(3), 1957–2011, doi:10.1021/cr2001756, 2012.
1092
1093 Zhao, J., Eisele, F. L., Titcombe, M., Kuang, C. and McMurry, P. H.: Chemical ionization mass
1094 spectrometric measurements of atmospheric neutral clusters using the cluster-CIMS, *J. Geophys.*
1095 *Res.*, 115(D8), 1–19, doi:10.1029/2009jd012606, 2010.
1096
1097

1098 **FIGURE LEGENDS:**

1099

1100 **Figure 1:** Average SMPS contour plots for (a) non-event days, (b) full-event days and (c) burst-
1101 event days.

1102

1103 **Figure 2:** Box plots for days of non-event, full-event and burst-event, showing (a) condensation
1104 sink, (b) temperature, and (c) global radiation from hourly data. “Full-event” and “burst-
1105 event” include data across the entire day.

1106

1107 **Figure 3:** Box plots for days of non-event, full-event and burst-event, showing (a) sulphuric acid,
1108 (b) C₂ and C₄ amines, as clustered with the nitrate dimer and trimer, and (c) summed
1109 HOM concentration from C₅₊ from hourly data. Units for ammonia + amines are
1110 normalised counts, as no calibration was performed. Event days include data across the
1111 full event day.

1112

1113 **Figure 4:** Formation rate (J_{1.9}) plotted against sulphuric acid monomer concentration, coloured by
1114 condensation sink. Circles represent burst-events, squares represent full events. Data is
1115 for hourly averages across NPF periods, typically within the hours 08:00 – 16:00. Slope
1116 of the line = $4.9 \cdot 10^{-5} \text{ s}^{-1}$. Error bars represent systematic uncertainties on [H₂SO₄] and
1117 J_{1.9}.

1118

1119 **Figure 5:** Formation rate plotted against sulphuric acid monomer concentration for data collected
1120 from Barcelona. Tan circles represent burst-events, purple squares represent full events.
1121 as well as that for the H₂SO₄-H₂O (blue inverted triangles), H₂SO₄-NH₃-H₂O (yellow
1122 inverted triangles), H₂SO₄-DMA-H₂O (pink triangles), and H₂SO₄-BioOxOrg-H₂O
1123 (brown diamonds) systems from the CLOUD chamber (Kürten et al., 2018 Kirkby et al.,
1124 2011; Riccobono et al., 2014). CLOUD chamber experiments were performed at 278 K
1125 and 38 – 39 % RH. Data is for hourly averages across NPF periods, typically within the
1126 hours 08:00 – 16:00. Error bars represent systematic uncertainties on [H₂SO₄] and J_{1.9}.

1127

1128 **Figure 6:** Sulphuric acid dimer concentration plotted against monomer concentration, showing
1129 burst-event periods (tan circles), full event periods (purple squares), non-event periods
1130 (green inverted triangles), and the ratio of sulphuric acid dimer:monomer in the CLOUD
1131 chamber for the H₂SO₄-H₂O-DMA system (pink triangles) (Almeida et al., 2013).
1132 Dashed line represents the dimer concentration produced by ion induced clustering in the
1133 chemical ionization unit (Zhao et al., 2010). CLOUD chamber experiments were
1134 performed at 278 K and 38 – 39 % RH. Data is for hourly averages across NPF periods,
1135 typically within the hours 08:00 – 16:00. Error bars represent systematic uncertainties on
1136 [H₂SO₄] and [(H₂SO₄)₂].

1137

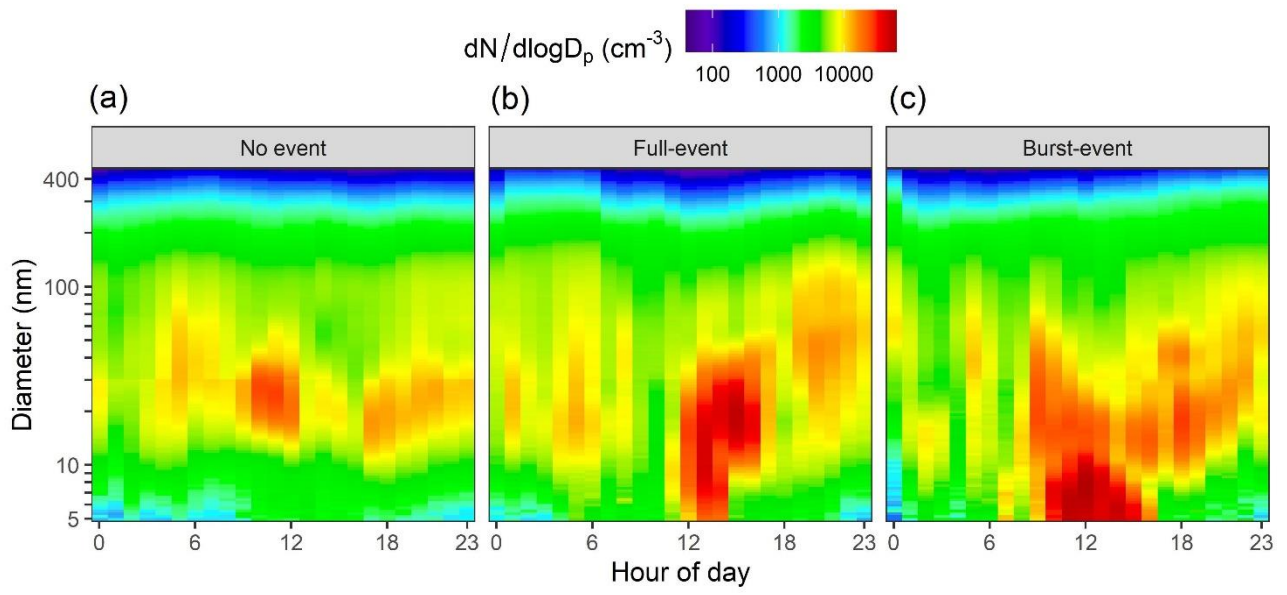
1138 **Figure 7:** Influencing factors on HOM concentration, showing (a) C₅₋₁₀ HOM concentration plotted
1139 against temperature, coloured by global radiation. Ellipsis shows 95% confidence on a
1140 multivariate t-distribution. (b) HOM concentration by carbon number plotted against
1141 parent VOC mixing ratio. These are segregated by carbon number/VOC, i.e. C₇ HOMs
1142 plotted against toluene, under the assumption that toluene oxidation is the main producer
1143 of C₇ HOMs. Time for both plots is of hourly time resolution.

1144

1145 **Figure 8:** Concentrations of all oxygenated organic molecules and HOMs binned to integer
1146 Log₁₀(C*) values, coloured by DBE.

1147

1148 **Figure 9:** Mass defect plots for (a) non-event, (b) full-event, and (c) burst-event periods, data
1149 taken from 10:00 – 15:00 on the days 11/07/2018, 16/07/2018 and 15/07/2018
1150 respectively. Size corresponds to mass spectral peak area. Ions are coloured according
1151 to identified chemical composition. *Blue* points correspond to HOMs containing all
1152 organic species with ≥ 5 carbon atoms and ≥ 6 oxygen atoms, and an O:C ratio of >0.6 .
1153 *Purple* points correspond to the same but for species containing 1-2 nitrogen atoms.
1154 Species not meeting this HOM criteria were classed generally as OVOCs which are
1155 coloured *brown*, with the nitrogen containing OVOCs coloured *orange*. Sulphur acids
1156 (*red*) include ions HSO_4^- , CH_3SO_3^- and SO_5^- , as well as the sulphuric acid dimer. Iodine
1157 acids (*green*) contains both IO_3^- and I^- (the latter presumably deprotonated hydrogen
1158 iodide). Unidentified points are left uncoloured.
1159

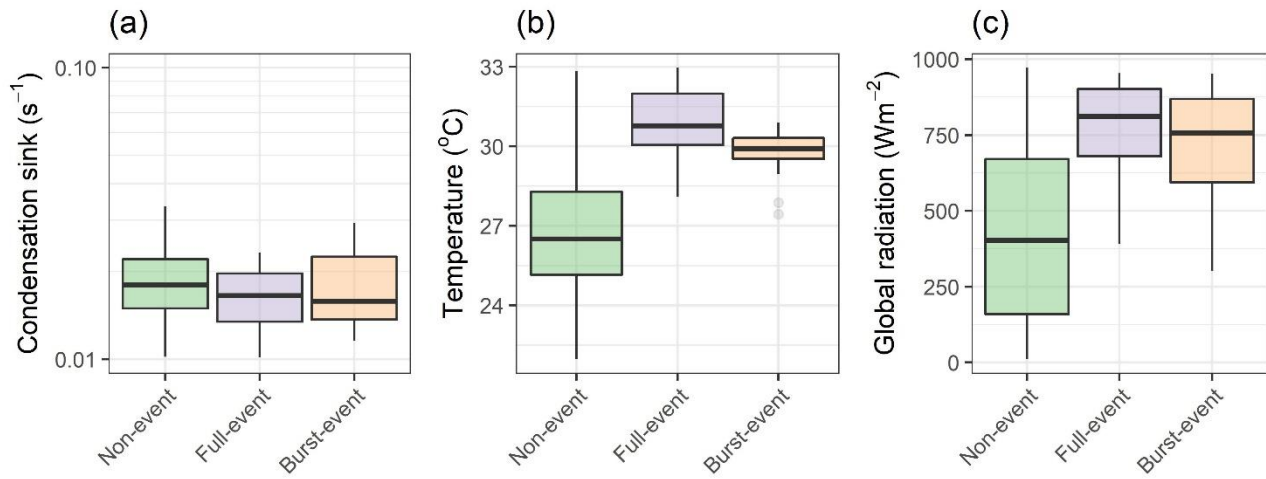


1161

1162 **Figure 1:** Average SMPS contour plots for (a) non-event days, (b) full-event days and (c) burst-event
1163 days.

1164

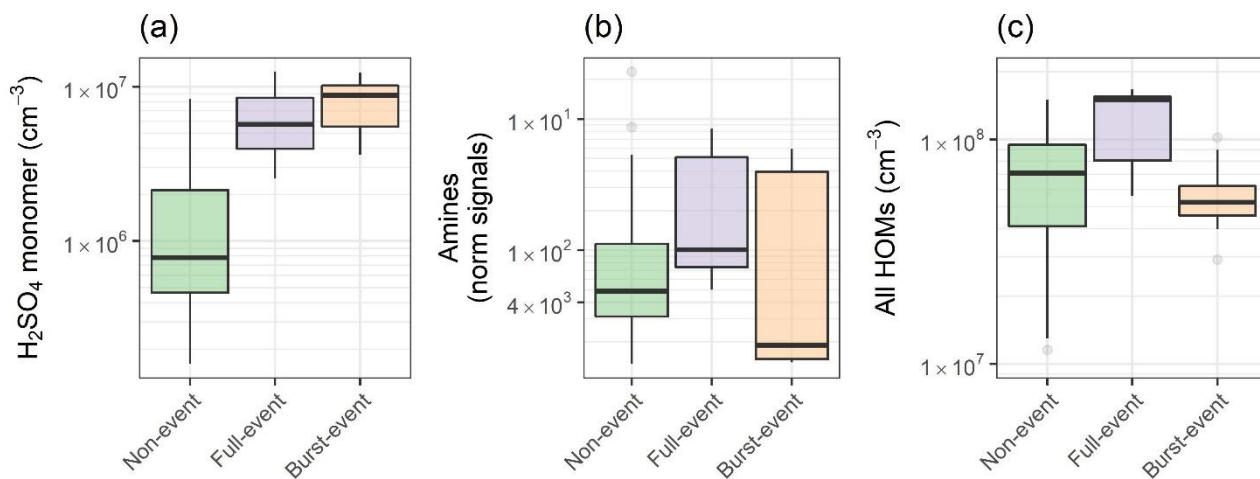
1165



1167

1168 **Figure 2:** Box plots for days of non-event, full-event and burst-event, showing (a) condensation sink,
 1169 (b) temperature, and (c) global radiation from hourly data. “Full-event” and “burst-event” include
 1170 data across the entire day.

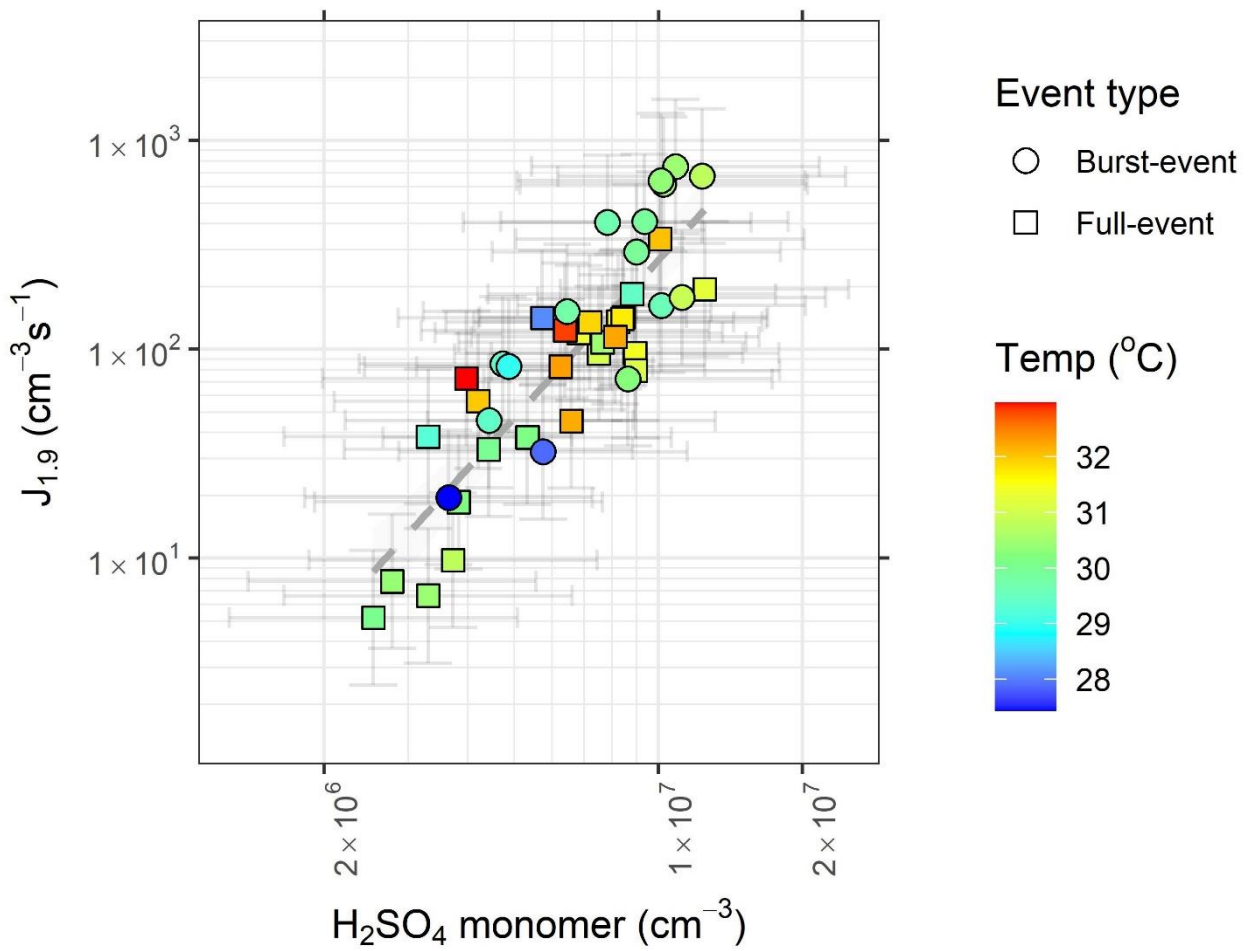
1171



1173

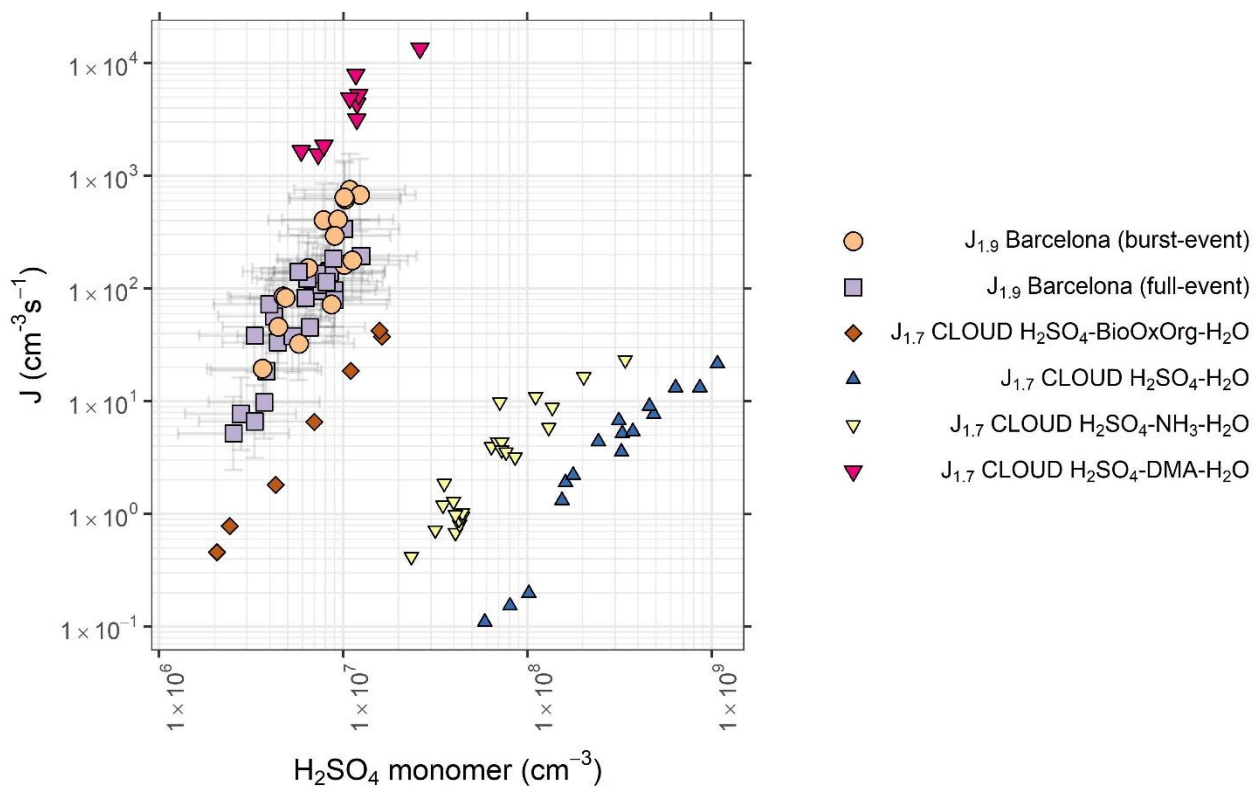
1174 **Figure 3:** Box plots for days of non-event, full-event and burst-event, showing (a) sulphuric acid, (b)
 1175 C_2 and C_4 amines, as clustered with the nitrate dimer and trimer, and (c) summed HOM concentration
 1176 from C_{5+} from hourly data. Units for ammonia + amines are normalised counts, as no calibration was
 1177 performed. Event days include data across the full event day.

1178



1180

1181 **Figure 4:** Formation rate ($J_{1.9}$) plotted against sulphuric acid monomer concentration, coloured by
 1182 condensation sink. Circles represent burst-events, squares represent full events. Data is for hourly
 1183 averages across NPF periods, typically within the hours 08:00 – 16:00. Slope of the line = $4.9 \cdot 10^{-5} \text{ s}^{-1}$
 1184 ¹. Error bars represent systematic uncertainties on $[\text{H}_2\text{SO}_4]$ and $J_{1.9}$

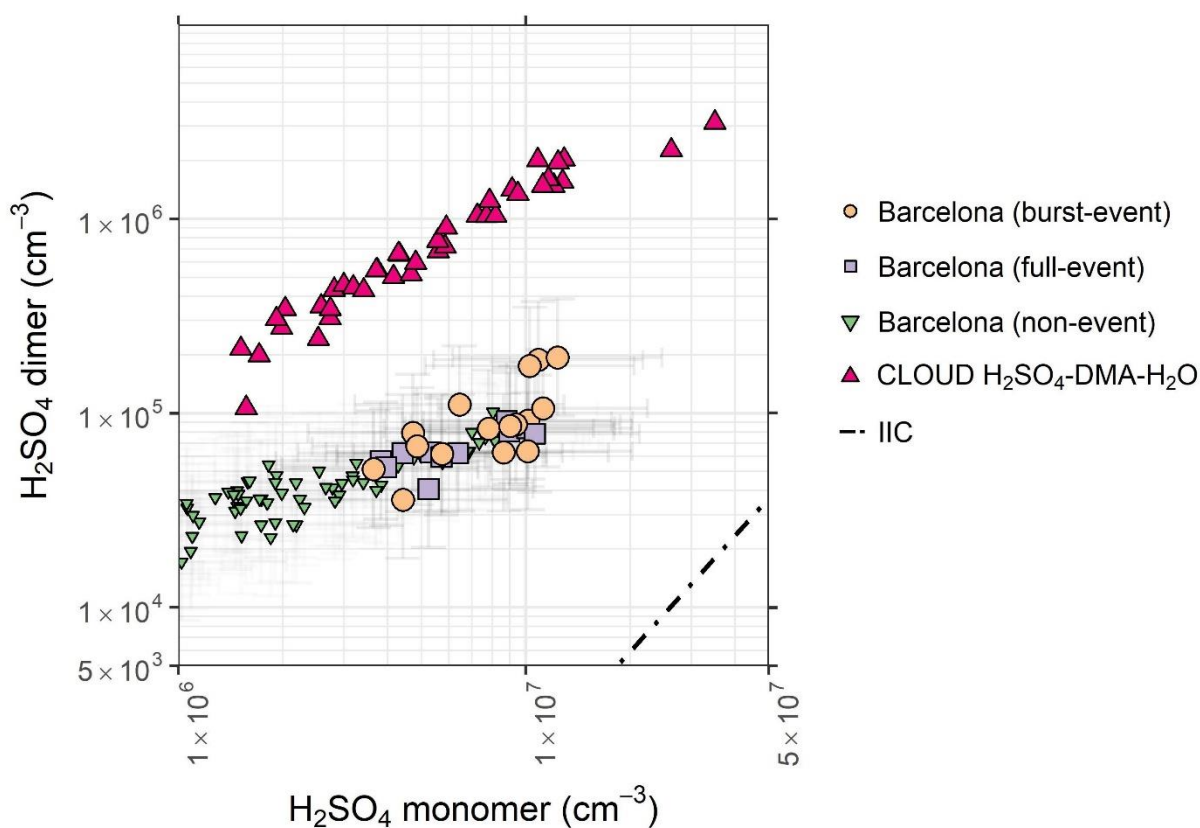


1185

1186 **Figure 5:** Formation rate plotted against sulphuric acid monomer concentration for data collected
 1187 from Barcelona. Tan circles represent burst-events, purple squares represent full events. as well as
 1188 that for the H₂SO₄-H₂O (blue inverted triangles), H₂SO₄-NH₃-H₂O (yellow inverted triangles),
 1189 H₂SO₄-DMA-H₂O (pink triangles), and H₂SO₄-BioOxOrg-H₂O (brown diamonds) systems from the
 1190 CLOUD chamber (Kürten et al., 2018 Kirkby et al., 2011; Riccobono et al., 2014). CLOUD
 1191 chamber experiments were performed at 278 K and 38 – 39 % RH. Data is for hourly averages
 1192 across NPF periods, typically within the hours 08:00 – 16:00. Error bars represent systematic
 1193 uncertainties on [H₂SO₄] and J_{1.9}.

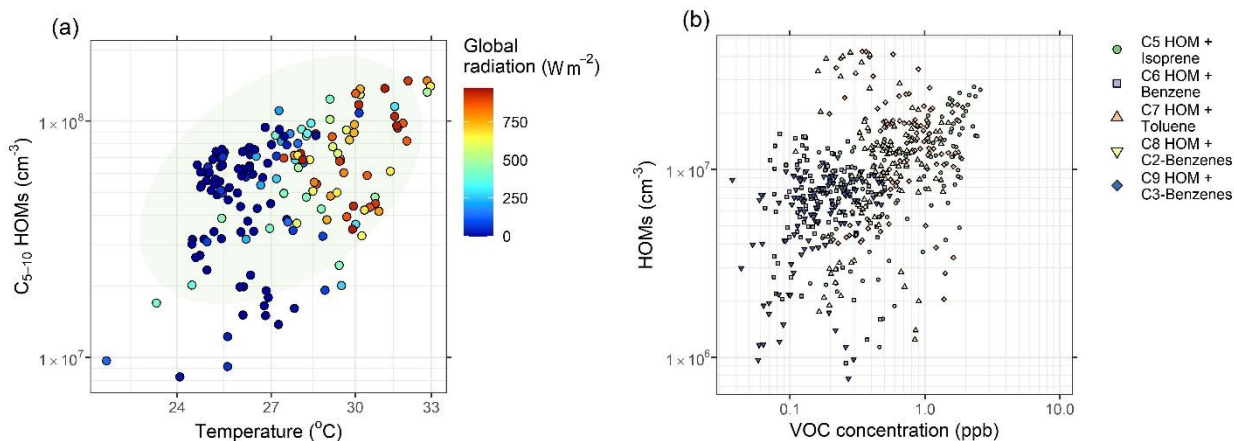
1194

1195



1196
 1197 **Figure 6:** Sulphuric acid dimer concentration plotted against monomer concentration, showing burst-
 1198 event periods (tan circles), full event periods (purple squares), non-event periods (green inverted
 1199 triangles), and the ratio of sulphuric acid dimer:monomer in the CLOUD chamber for the H_2SO_4 -
 1200 H_2O -DMA system (pink triangles) (Almeida et al., 2013). Dashed line represents the dimer
 1201 concentration produced by ion induced clustering in the chemical ionization unit (Zhao et al., 2010).
 1202 CLOUD chamber experiments were performed at 278 K and 38 – 39 % RH. Data is for hourly
 1203 averages across NPF periods, typically within the hours 08:00 – 16:00. Error bars represent systematic
 1204 uncertainties on $[\text{H}_2\text{SO}_4]$ and $[(\text{H}_2\text{SO}_4)_2]$.

1205

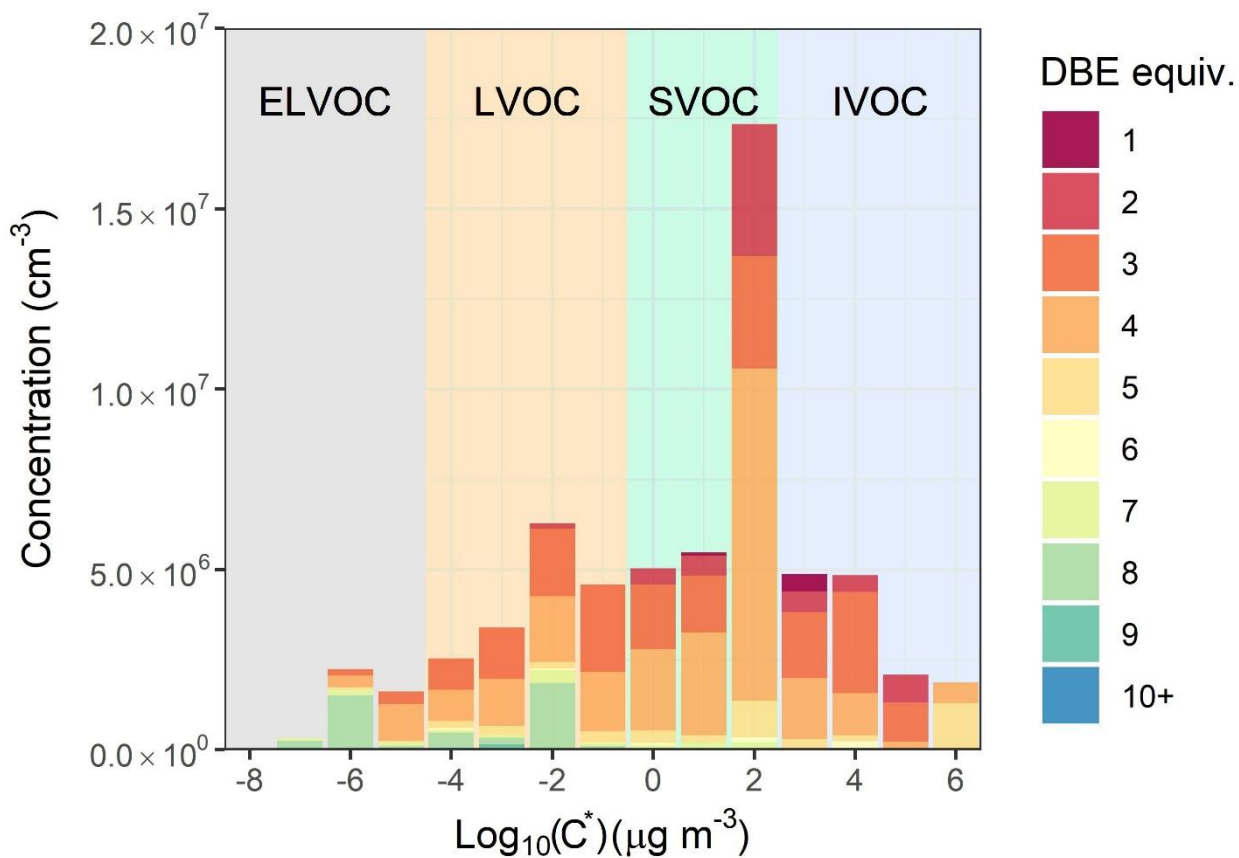


1207

1208 **Figure 7:** Influencing factors on HOM concentration, showing (a) C₅₋₁₀ HOM concentration plotted
 1209 against temperature, coloured by global radiation. Ellipsis shows 95% confidence on a multivariate
 1210 t-distribution. (b) HOM concentration by carbon number plotted against parent VOC mixing ratio.
 1211 These are segregated by carbon number/VOC, i.e. C₇ HOMs plotted against toluene, under the
 1212 assumption that toluene oxidation is the main producer of C₇ HOMs. Time for both plots is of hourly
 1213 time resolution.

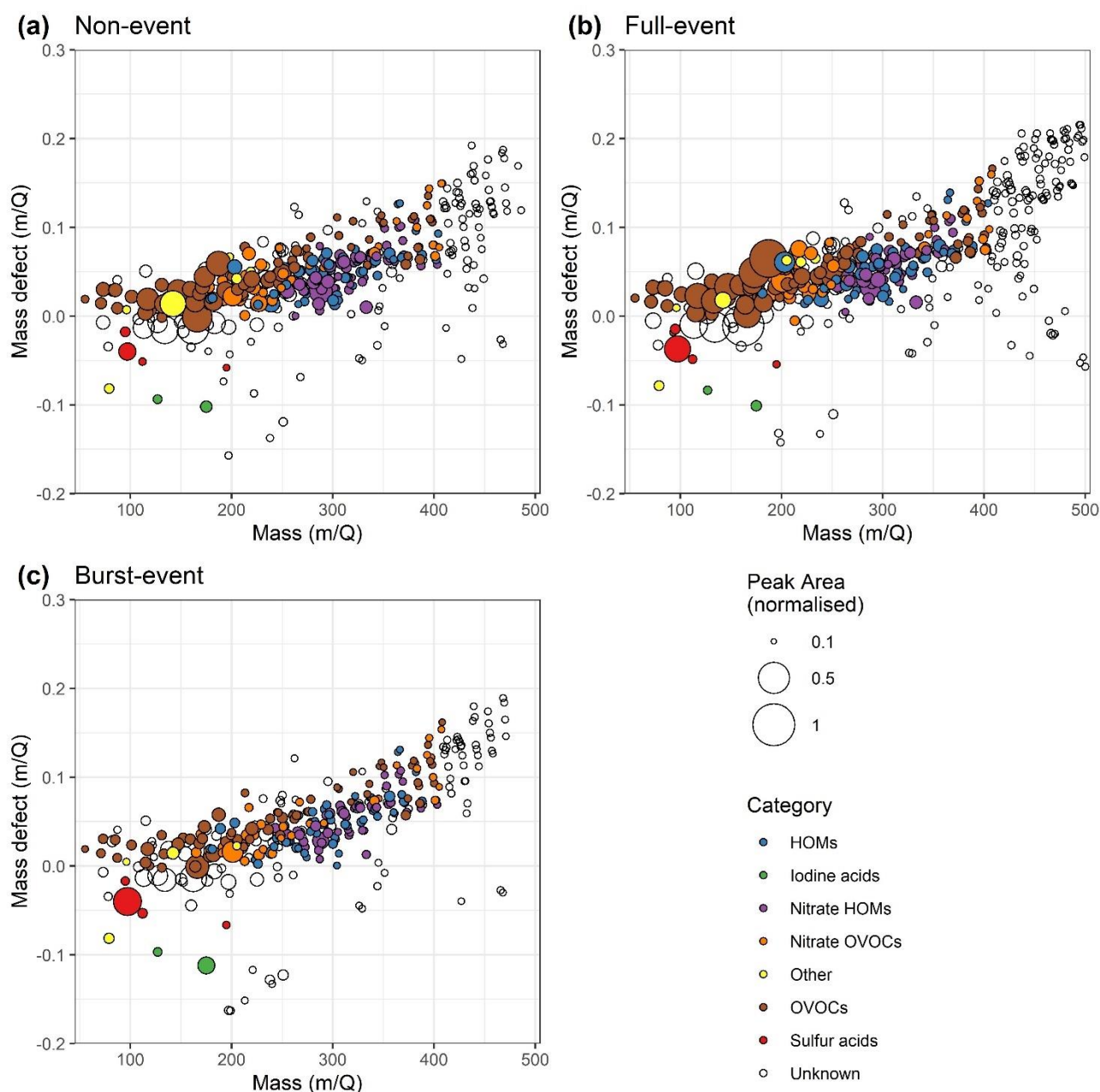
1214

1215



1216

1217 **Figure 8:** Concentrations of all oxygenated organic molecules and HOMs binned to integer $\text{Log}_{10}(C^*)$
1218 values, coloured by DBE.



1219

1220 **Figure 9:** Mass defect plots for (a) non-event, (b) full-event, and (c) burst-event periods, data taken
 1221 from 10:00 – 15:00 on the days 11/07/2018, 16/07/2018 and 15/07/2018 respectively. Size
 1222 corresponds to mass spectral peak area. Ions are coloured according to identified chemical
 1223 composition. *Blue* points correspond to HOMs containing all organic species with ≥ 5 carbon atoms
 1224 and ≥ 6 oxygen atoms, and an O:C ratio of >0.6 . *Purple* points correspond to the same but for species
 1225 containing 1-2 nitrogen atoms. Species not meeting this HOM criteria were classed generally as
 1226 OVOCs which are coloured *brown*, with the nitrogen containing OVOCs coloured *orange*. Sulphur
 1227 acids (*red*) include ions HSO_4^- , CH_3SO_3^- and SO_5^- , as well as the sulphuric acid dimer. Iodine acids
 1228 (*green*) contains both IO_3^- and I^- (the latter presumably deprotonated hydrogen iodide). Unidentified
 1229 points are left uncoloured.

1230